

Chaotic Mixing in Three Dimensional Porous Media

Daniel R. Lester^{1†}, Marco Dentz²
and Tanguy Le Borgne³

¹School of Civil, Environmental and Chemical Engineering, RMIT University, 3000 Melbourne, Victoria, Australia

²Spanish National Research Council (IDAEA-CSIC), 08034 Barcelona, Spain

³Geosciences Rennes, UMR 6118, Université de Rennes 1, CNRS, 35042 Rennes, France

(Received ?; revised ?; accepted ?. - To be entered by editorial office)

Under steady flow conditions, the topological complexity inherent to all random 3D porous media imparts complicated flow and transport dynamics. It has been established that this complexity generates persistent chaotic advection via a three-dimensional (3D) fluid mechanical analogue of the baker's map which rapidly accelerates scalar mixing in the presence of molecular diffusion. Hence pore-scale fluid mixing is governed by the interplay between chaotic advection, molecular diffusion and the broad (power-law) distribution of fluid particle travel times which arise from the non-slip condition at pore walls. To understand and quantify mixing in 3D porous media, we consider these processes in a model 3D open porous network and develop a novel stretching continuous time random walk (CTRW) which provides analytic estimates of pore-scale mixing which compare well with direct numerical simulations. We find that chaotic advection inherent to 3D porous media imparts scalar mixing which scales exponentially with longitudinal advection, whereas the topological constraints associated with 2D porous media limits mixing to scale algebraically. These results decipher the role of wide transit time distributions and complex topologies on porous media mixing dynamics, and provide the building blocks for macroscopic models of dilution and mixing which resolve these mechanisms.

Key words: Lagrangian chaos, porous media, mixing, scalar transport

1. Introduction

All porous media, whether random or ordered, granular or networked, heterogeneous or homogeneous, are typified by the geometric and topological complexity of the pore-space (Scholz *et al.* 2012; Vogel 2002). This pore-space plays host to a wide range of fluid-borne processes including transport, mixing and dispersion, chemical reaction and microbiological activity, all of which are influenced by the flow structure and transport properties (Metcalf *et al.* 2012; Dentz *et al.* 2011; de Barros *et al.* 2012; Chiogna *et al.* 2012). Pore-scale fluid mixing plays a key role in the control of both fluid-fluid reactions (e.g. redox processes) and fluid-solid reactions (e.g. precipitation-dissolution processes), which are of importance for a range of subsurface operations, including CO₂ sequestration, contaminant remediation or geothermal dipoles management. Whilst pore-scale flows are often smooth and steady (typically Stokesian or laminar), the inherent topo-

† Email address for correspondence: daniel.lester@rmit.edu.au

logical complexity of the pore-space renders upscaling transport and mixing processes a challenging task.

Because of their fundamental role in driving chemical reactions, mixing processes have received increasing attention in recent years in the context of porous media flows (Dentz *et al.* 2011). Two-dimensional laboratory experiments (Gramling *et al.* 2002; Tartakovsky *et al.* 2008; de Anna *et al.* 2014) and theoretical and modeling studies (Battiato *et al.* 2009) have shown that upscaled chemical kinetics are not captured by classical macro-dispersion theories due to incomplete mixing at the pore scale. This points to a need for predictive theories for pore-scale concentration statistics which are couched in terms of the underlying medium properties. Lamellar mixing theories, developed in the context of turbulent flows (Villermaux & Duplat 2003; Duplat & Villermaux 2008; Duplat *et al.* 2010), have been applied and extended for the prediction of concentration statistics in two-dimensional (2D) Darcy scale heterogeneous porous media (Le Borgne *et al.* 2013, 2015). A central element of this theory is to quantify the link between fluid stretching and mixing. In this context, linking the pore network topological properties to mixing dynamics is an essential step, which we explore in this study.

While the topological constraints associated with the Poincaré-Bendixson theorem limit fluid stretching in two-dimensional (2D) steady flows to be algebraic, in three-dimensional (3D) steady flows much richer behaviour is possible. Indeed, the topological complexity inherent to all three dimensional random porous media has been shown to induce chaotic advection under steady flow conditions via a 3D fluid mechanical analogue of the baker’s map (Lester *et al.* 2013). Such chaotic Lagrangian dynamics are well-known to rapidly accelerate diffusive mixing and scalar dissipation (Ottino 1989), yet have received little attention with respect to pore-scale flow. From the perspective of transport dynamics, the distribution of pore sizes and shapes, together with no-slip boundary conditions at the pore walls, are known to impart non-Gaussian pore velocity distributions (Moroni & Cushman 2001; Bijeljic *et al.* 2011; Kang *et al.* 2014; Holzner *et al.* 2015), which lead to a rich array of dispersion phenomena ranging from normal to super-diffusive. The continuous time random walk (CTRW) approach (Berkowitz *et al.* 2006) has been used to model this behaviours (Bijeljic *et al.* 2003; Le Borgne *et al.* 2011; de Anna *et al.* 2013; Kang *et al.* 2014; Holzner *et al.* 2015) based on the transit time distributions over characteristic pore lengths, which reflect the distribution of pore velocities. The interplay of wide transit time distributions and chaotic advection at the pore-scale impacts both macroscopic transport and dispersion as well as pore-scale dilution.

Pore-scale chaotic advection has been shown Lester *et al.* (2014) to significantly suppress longitudinal dispersion arising from the no-slip wall condition due to transverse mixing generating an analogue of the Taylor-Aris mechanism. Conversely, the wide transit time distributions are expected to have a drastic impact on the dynamics of mixing in conjunction with chaotic advection as the transit times set the timescales over which significant stretching of a material fluid element occurs. While the impact of broad transit time distributions on the spatial spreading of transported elements is well understood, their control on mixing dynamics is still an open question. As shown in (Lester *et al.* 2014), Lagrangian chaos generates ergodic particle trajectories at the pore-scale, and the associated decaying correlations allows the advection process to be modelled as a stochastic process. During advection through the pore-space, fluid elements undergo punctuated stretching and folding (transverse to the mean flow direction) events at stagnation points, leading to persistent chaotic advection in random porous media. Such dynamics have been captured in an idealized 3D random pore network model which comprises of a periodic network of uniform-sized pores which alternately branch and merge in the mean flow direction, leading to a high number density of stagnation points local to these pore

junctions which generate fluid stretching. Whilst highly idealized, this network model contains basic features common to all porous media, namely topology-induced chaotic advection and no-slip boundary conditions, and so represents the minimum complexity inherent to all porous media.

In this paper, we develop a novel stretching CTRW which captures the advection and deformation of material elements through the porous matrix. Closure of this CTRW model in conjunction with a 1D advection-diffusion equation (ADE) describing diffusion transverse to highly striated, lamellar concentration distributions generated by pore-scale chaotic advection facilitates quantification of mixing and dispersion of scalar fields under the action of combined chaotic advection and molecular diffusion both within the pore space and across the macroscopic network. This formalism allows prediction of concentration PDF evolution within the pore-space and quantification of the impact of chaotic advection.

To simplify exposition, we first consider the somewhat artificial case of a steady state pore-scale mixing and dispersion of a concentration field which is heterogeneous at the pore-scale but homogeneous at the macro-scale continuously injected across all pores in a plane transverse to the mean flow direction. These results are then extended to the more realistic situation of the evolution of a solvent plume which is continuously injected as a point source. We compare these predictions for three distinctly different porous networks, a random 3D porous network which gives rise to Lagrangian chaos, an ordered 3D porous network which generates maximum fluid stretching, and an ordered 2D network which gives rise to non-chaotic dynamics. Hence the impact of both network topology and structure upon pore-scale mixing and dispersion is quantified. These results form a quantitative basis for upscaling of pore-scale dynamics to macroscopic mixing and transport models, and establish the impacts of ubiquitous chaotic mixing in 3D random porous media.

The paper is organized as follows; the mechanisms leading to topological mixing in 3D porous media are briefly reviewed in § 2, followed by a description of the 3D open porous network model in § 3. Fluid stretching in this model network is considered in § 4, from which a stretching CTRW model is derived in § 5. This model is then applied to quantify mixing in § 6, and the implications for the evolution of the concentration PDF, mixing scale and dispersion are considered in § 7. The overall results are discussed in § 8 and finally conclusions are made in § 9.

2. Topologically-Induced Fluid Deformation in 3D Porous Media

Topological complexity is a defining feature of all porous media - from granular and packed media to fractured and open networks - these materials are typified by a highly connected pore-space within which the flow of continua arise. Such topological complexity is characterised by the Euler characteristic χ (related to the topological genus g as $\chi = 2(1 - g)$) which measures the connectivity of the pore-space (Vogel 2002) as

$$\chi = N - C + H, \quad (2.1)$$

where N is the number of pores, C the number of redundant connections and H the number of completely enclosed cavities. For porous media it is meaningful to consider the average number density of these quantities, where from computer tomography studies (Vogel 2002) it is found that typically N is large whilst C , H are small. Hence the number density of the Euler characteristic χ is uniformly found to be strongly negative (Scholz *et al.* 2012; Vogel 2002), reflecting the basic topological complexity which typifies all porous media. When a continuous fluid is advected through such media, a large

number of stagnation points (non-degenerate equilibrium points) arise at the fluid/solid boundary as a direct result of this topological complexity. These stagnation points \mathbf{x}_p are zeros of the skin friction vector field $\mathbf{u}(\mathbf{x})$ on the 2D boundary $\partial\mathcal{D}$ of the fluid domain \mathcal{D} , where $\mathbf{u}(\mathbf{x})$ may be defined as

$$\mathbf{u}(x_1, x_2, x_3) := \frac{\partial \mathbf{v}}{\partial x_3}. \quad (2.2)$$

Here $\mathbf{v}(x_1, x_2, x_3)$ is the fluid velocity field, x_3 is the coordinate normal to the fluid boundary $\partial\mathcal{D}$ and x_1, x_2 are orthogonal coordinates tangent to this boundary. Whilst different definitions of the skin friction are possible (Surana *et al.* 2006; de Winkel & Bakker 1988; Chong *et al.* 2012), these are all equivalent on the boundary $\partial\mathcal{D}$, as is the topology of the flow structure in the fluid domain \mathcal{D} . The Poincaré-Hopf theorem provides a direct relationship between the nature of the critical points \mathbf{x}_p and the pore-space topology, such that the sum of the indices γ_p of critical points \mathbf{x}_p is related to the topological genus g and Euler characteristic χ as

$$\sum_p \gamma_p(\mathbf{x}_p) = 2(1 - g) = \chi, \quad (2.3)$$

where the index γ_p equals -1 for saddle-type zeros, +1 for node-type zeros and 0 for null zeros of the skin-friction field. Hence $|\chi|$ represents a lower bound for the number density of stagnation points under steady 3D Stokes flow, and these points impart significant fluid stretching into the local fluid domain. Digital imaging studies (Vogel 2002) measure the Euler characteristic across a broad range of porous media, from granular to networked, and find χ to be strongly negative, with number densities of the order $\sim 200\text{--}500 \text{ mm}^{-3}$. This large number density of stagnation points imparts a series of punctuated stretching events as the fluid continuum is advected through the pore-space. A relevant question is what role these stretching events play with respect to transport and mixing in porous media?

Stagnation points play a critical role with respect to the Lagrangian dynamics of 3D steady flows, as it is at these points that the formal analogy between transport in steady 3D volume-preserving flows and 1 degree-of-freedom Hamiltonian systems breaks down (Bajer & Moffatt 1990; Bajer 1994) (such that the steady 3D dynamical system can no longer be expressed as an analogous unsteady 2D system), and such points are widely (Mezić & Wiggins 1994; Wiggins 2010) implicated in the creation of non-trivial Lagrangian dynamics. MacKay (1994, 2008) proposes that the stable \mathcal{W}^s and unstable \mathcal{W}^u manifolds which respectively correspond to the fluid contraction and stretching directions around stagnation points (shown in Figure 1) form the “skeleton” of the flow, a set of surfaces of minimal transverse flux which organize transport within the fluid domain. If these manifolds which project into the fluid bulk are two-dimensional (hence co-dimension one), they form essentially impenetrable barriers which organise fluid transport and mixing.

Whilst the detailed dynamics of stagnation points and lines and their associated manifolds is more complicated (Surana *et al.* 2006) than described herein, the main point is that the dimensionality of the stable or unstable manifolds which are normal to the surface $\partial\mathcal{D}$ is dictated by the topological index γ_p or stagnation point type (saddle, node, null). Fluid deformation local to stagnation points \mathbf{x}_p is quantified by the linearized skin friction tensor \mathcal{A} , the components a_{ij} of which are given by the expansion

$$u_i = \sum_{j=1}^3 a_{ij}(x_j - x_{p,j}) + \mathcal{O}((x_j - x_{p,j})^2). \quad (2.4)$$

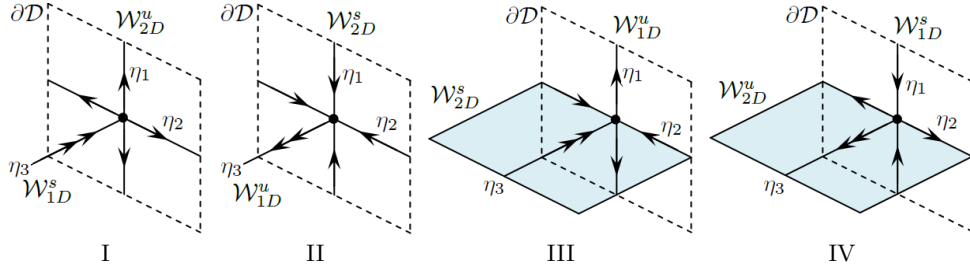


FIGURE 1. Type I-IV non-degenerate equilibrium points (with stagnation points I,III and reattachment points II, IV) on the boundary $\partial\mathcal{D}$ and associated stable and unstable manifolds \mathcal{W}^s , \mathcal{W}^u . The double arrows reflect the sum $\eta_1 + \eta_2 + 2\eta_3 = 0$.

Several workers (de Winkel & Bakker 1988; Chong *et al.* 2012) have derived the normal form of the skin friction tensor \mathcal{A} around a non-degenerate equilibrium point \mathbf{x}_p in an incompressible flow as

$$\mathcal{A} = \begin{pmatrix} a_{11} & a_{12} & a_{13} \\ a_{21} & a_{22} & a_{23} \\ 0 & 0 & -\frac{1}{2}(a_{11} + a_{22}) \end{pmatrix}, \quad (2.5)$$

where the eigenvalues η of \mathcal{A} satisfy $\eta_1 + \eta_2 + 2\eta_3 = 0$, where η_1, η_2 are the eigenvalues in the skin friction boundary (with $\eta_1 \leq \eta_2$), and η_3 is the interior eigenvalue. Hence $\eta_3 > 0$ for separation points and $\eta_3 < 0$ for reattachment points, and non-degenerate equilibrium points consist of one stable and two unstable eigenvalues or vice versa. As the linearisation (2.5) indicates that the tangent boundary is an invariant plane, there exist four basic types of equilibrium points as shown in Figure 1:

- type I separation point $\eta_3 > 0$, attractor for the skin friction field $\eta_1 < 0, \eta_2 < 0$,
- type II reattachment point $\eta_3 < 0$, repeller for the skin friction field $\eta_1 > 0, \eta_2 > 0$,
- type III separation point $\eta_3 > 0$, saddle for the skin friction field $\eta_1 < 0, \eta_2 > 0$,
- type IV reattachment point $\eta_3 < 0$, saddle for the skin friction field $\eta_1 < 0, \eta_2 > 0$.

Type I and II points are of node type, whilst type III and IV points are saddle points (with $\eta_1 < 0, \eta_2 > 0$) where the respective stable and unstable invariant manifolds which propagate into the fluid interior are two-dimensional, and so form surfaces of locally minimal flux which act as barriers to transport. Due to the strongly negative Euler characteristic common to most porous media, then from (2.3) such media admit a high number density of saddle-type points under steady 3D Stokes flow. Figure 2 illustrates these concepts for a pore branch (a) and merger (b) (the union of which is termed a couplet) in an open porous network. Here, the reattachment (stagnation) point in (a) ((b)) must arise due to the basic topology of the pore branch (merger), and this point of saddle type III (IV) gives rise to a 2D manifold \mathcal{W}_{2D}^s (\mathcal{W}_{2D}^u) which propagates into the fluid domain. It is important to note that whilst the geometry of pore branches and merges may vary significantly, the basic topology shown in Figure 2 is universal to almost all porous media, whether porous networks or granular media.

The interaction of the 2D manifolds ($\mathcal{W}_{2D}^s, \mathcal{W}_{2D}^u$) in the fluid bulk govern fluid transport and mixing. As is well-known from classical studies from Hamiltonian chaos, if two co-dimension 1 manifolds intersect transversely (via heteroclinic or homoclinic connections) then chaotic dynamics result, whereas smooth connections yield regular Lagrangian dynamics. For the pore junction shown in Figure 2, significant fluid stretching (compression) occurs transverse to the 2D manifolds (as indicated by the transverse 1D manifolds in Figure 1), whilst folding of material elements occurs due to downstream advection

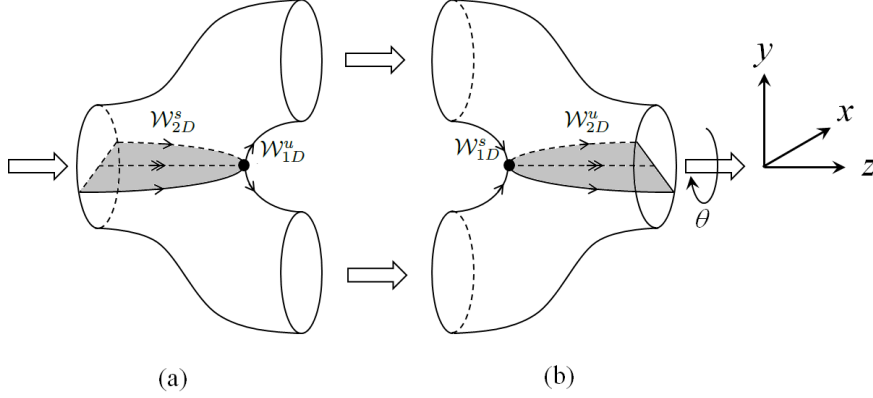


FIGURE 2. Schematic of pore branch (a) and pore merger (b) elements, with non-degenerate equilibrium stagnation (separation) points shown and associated 2D unstable (stable) manifolds, representing surfaces of locally minimum flux. Note the transverse orientation of angle θ of the minimum flux surfaces.

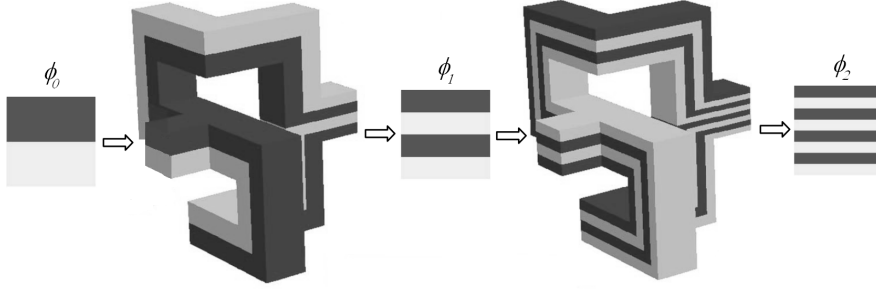


FIGURE 3. Schematic of the baker's flow, a 3D fluid mechanical implementation of the baker's map arising from non-trivial pore branching and merging. Adapted from Carrière (Carrière 2007)

local to the stagnation points. These actions are the constituent motions of the Smale horseshoe map, a hallmark of chaotic dynamics in continuous systems. If the 2D manifolds $\mathcal{W}_{2D}^s, \mathcal{W}_{2D}^u$ in Figure 2 are oriented transversely (as indicated by the angle θ), then persistent fluid stretching and folding can occur, whereas for symmetric connections ($\theta = 0$), these deformations cancel and the symmetry of Lagrangian stretching histories leads to non-chaotic dynamics.

The dynamics of topologically complex systems is considered by MacKay (2001), who studied flow within a closed domain topologically equivalent to a connected pore branch and merger (Figure 2) with the merger outlet also glued to the branch inlet, forming a closed domain of genus 2. As the topology of this closed domain is equivalent to that of the open domain in Figure 2 with periodic boundaries, we make no distinction between the two systems. This closed flow is termed a baker's flow, which is a 3D fluid mechanical analogue of the baker's map, an archetypical chaotic map in Hamiltonian dynamics. This analogy corresponds to the case $\theta = \pi/2$, where transverse stretching and compression in the pore branch/merger leads to stretching and folding akin to the cutting and stacking of the Baker's map. MacKay (2001) shows that whilst this flow is not structurally stable, it is a volume-preserving analogue of the Lorentz system which is robustly mixing in the

right parameter regime. This contention is supported by the numerical results of Carrière (2007), who considers 3D steady Stokes flow in a periodic duct with repeat branches and mergers as shown in Figure 3. This flow is analogous to the pore couplet in Figure 2 with $\theta = \pi/2$, and generates almost globally chaotic dynamics (with the exception of small KAM tori due to reentrant vortices in duct corners) in the transverse Poincaré section (Carrière 2007). The measured Lyapunov exponent $\lambda_\infty = 0.68$ is very close to the theoretical upper bound $\lambda_{\max} = \ln 2$ for steady 3D flows. Hence, the skeleton of the flow can generate chaotic mixing in porous networks quantitatively similar to strong theoretic mixing (Sturman *et al.* 2008).

These basic mechanisms persist in granular and packed media, where the minimal flux surface associated with type III stagnation points wrap downstream around a particle cluster, and likewise the minimal flux surface associated with a type IV stagnation point wraps upstream. Again the orientation angle θ between these surfaces plays a critical role with respect to the persistence of fluid deformation. The disordered nature of random porous media ensures that the transverse orientation $\theta \neq 0$ condition is met with unit probability throughout the porous matrix, in which case the network structure imparts chaotic advection under steady flow conditions. Whilst porous media may exhibit other features such as surface roughness or pore tortuosity which may also generate chaotic advection (Jones *et al.* 1989; Ottino & Wiggins 2004), stagnation points are generic to topologically complex media, hence the mechanism described above represents a lower bound for chaotic dynamics inherent to porous media flow.

3. 3D Open Porous Network model

To study the impacts of such topology-induced chaotic advection upon transport and mixing in porous media, we consider a model 3D open porous network which consists of random network of connected pore junctions and mergers shown in Figure 2. We consider a non-trivial network of pore branches and mergers which is the simplest representation of an open porous network which may be considered homogeneous at the macroscale. To compose a random 3D network over the semi-infinite domain $\Omega : \mathbf{x} \in \mathbb{R}^3, z > 0$, we use the pore branch and merge elements (shown in Figure 2 (a), (b) respectively) to connect a series of so-called “mapping planes” oriented parallel to the (x, y) plane, distributed along the z -axis at integer multiples of the pore element length ℓ . Each mapping plane consists of an infinite number of reflections in the x, y directions of a periodic unit cell $x, y \in [0, 1] \times [0, 1]$ which contains $3N$ randomly-located non-overlapping pores, as shown in Figure 4. The location of the j -th pore in the i -th mapping plane is labelled $\mathbf{r}_{i,j} = (x_{i,j}, y_{i,j}, i\ell)$.

Of these $3N$ pores, N are randomly labelled as “branch” pores (i.e. pores which branch next in the positive z direction), and the remaining $2N$ pores are labelled as “merge pores” (i.e. those which are about to merge). A branch pore at plane i is connected to two merge pores at plane $i + 1$ by a pore branch element located between these planes, and conversely two branch pores at plane i are connected with a single merge pore at plane i by a pore merge element as per Figure 2. Connections between merge and branch pores in adjacent planes are made by identifying unique nearest neighbour groupings of a single merge pore in one plane and two branches in the adjacent plane (accounting for periodicity in the (x, y) -plane), such that all pores undergo sequential branching and merging as they propagate along the z -coordinate. Connections are restricted such that a pair of branch pores at plane i common to a single merge pore at $i - 1$ do not share the same merge pore at $i + 1$. This restriction both eliminates “degenerate” pore branch/merger couplings and ensures the orientation of connections is essentially random.

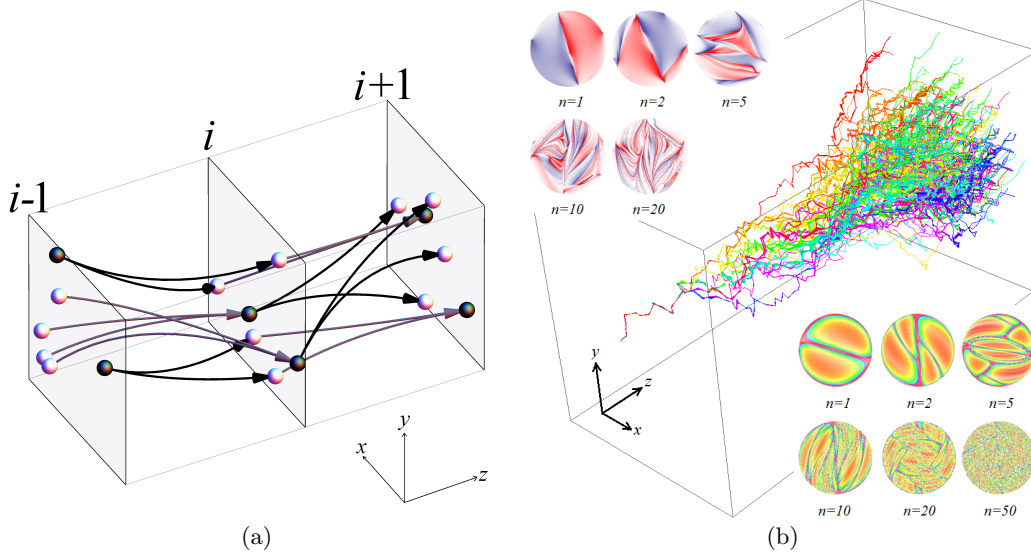


FIGURE 4. (a) Schematic of pore branches (black) and mergers (white) between mapping planes, with branch pores (black) and merge pores (white) shown. (b) (middle) Evolution of a typical non-diffusive dye plume in the pore network from continuous injection over a single inlet pore, (upper left) typical transverse distribution of non-diffusive coloured fluid particles with longitudinal pore number n , (lower right) typical distribution of residence times (pink = maximum, orange=minimum) with longitudinal pore number n .

To accommodate connections between the merge pore locations $\mathbf{r}_{m_1}, \mathbf{r}_{m_2}$ and the branch pore location \mathbf{r}_{b_1} at adjacent mapping planes, the pore branch and merge elements are rotated and stretched such that the $\hat{\mathbf{e}}_y, \hat{\mathbf{e}}_z$ vectors respectively are aligned along $\mathbf{r}_{m_1} - \mathbf{r}_{m_2}, \mathbf{r}_{b_1} - \frac{1}{2}(\mathbf{r}_{m_1} + \mathbf{r}_{m_2})$, and the element height and length (as oriented in Figure 2) respectively are re-scaled to $\|\mathbf{r}_{m_1} - \mathbf{r}_{m_2}\|, \|\mathbf{r}_{b_1} - \frac{1}{2}(\mathbf{r}_{m_1} + \mathbf{r}_{m_2})\|$. The orientation angle θ in the (x, y) plane of a pore branch/merge element is then

$$\theta = \arctan \left[\frac{(\mathbf{r}_{m_1} - \mathbf{r}_{m_2}) \cdot \hat{\mathbf{e}}_y}{(\mathbf{r}_{m_1} - \mathbf{r}_{m_2}) \cdot \hat{\mathbf{e}}_x} \right]. \quad (3.1)$$

Hence the set S of random pore locations $\mathbf{r}_{i,j}$ for $i = 0 : \infty, j = 1 : 3N$ completely defines a realization of the 3D open porous network, and the set of all realizations \mathcal{S} of the porous network form an ensemble which is ergodic and stationary. Due to the elimination of degenerate pore branch/merger couplings, the distribution of orientation angles θ are uncorrelated across and within mapping planes, and so transport within the 3D open porous network may be described by a multidimensional Markov process in space.

To model transport within the porous network, we consider fluid advection via the velocity field \mathbf{v} subject to Stokes flow $\mu \nabla^2 \mathbf{v} + \nabla p = 0$ within the pore branch element Ω driven by a differential pressure $p|_{z=0} - p|_{z=L} = \Delta p$, subject to no-slip boundary conditions $\mathbf{v} \cdot \mathbf{n}|_{\partial\Omega} = 0$. The flow field is calculated numerically to order 10^{-16} RMS accuracy using the finite-volume CFD package ANSYS-CFX with double precision calculations. The advection dynamics for passive tracer particles within the branch element Ω under Stokes flow can be represented by the spatial \mathcal{M}^* and temporal \mathcal{T}^* maps

$$\mathcal{M}^* : \{x_{r,i}, y_{r,i}\} \mapsto \{x_{r,i+1}, y_{r,i+1}\}, \quad (3.2)$$

$$\mathcal{T}^* : t_i \mapsto t_{i+1} \quad (3.3)$$

where $\{x_{r,i}, y_{r,i}\}$ are the x, y particle positions relative to the inlet pore of Ω (where $x_{r,i}^2 + y_{r,i}^2 = 0, 1$ respectively corresponds to the pore centre and boundary), and $\{x_{r,i+1}, y_{r,i+1}\}$ are the x, y particle positions relative to the outlet pore of Ω . Note that $x_{r,i+1}, y_{r,i+1}$ are independent of the specific outlet pore the particle travels to. Similarly, the temporal map \mathcal{T}^* describes the residence time from the inlet to outlet planes. From the CFD results, the exact maps $\mathcal{M}^*, \mathcal{T}^*$ are remarkably well approximated (within error $\epsilon \sim 10^{-3}$) by the simple analytic maps

$$\mathcal{M} : \{x_r, y_r\} \mapsto \begin{cases} \{x_r, 2y_r - \sqrt{1 - x_r^2}\} & \text{if } y_r > 0 \\ \{x_r, 2y_r + \sqrt{1 - x_r^2}\} & \text{if } y_r \leq 0 \end{cases}, \quad (3.4)$$

$$\mathcal{T} : t \mapsto t + \frac{1}{1 - x_r^2 - y_r^2}. \quad (3.5)$$

These approximate maps greatly simplify description of the advection dynamics in the pore branch element Ω and preserve the essential features of advective transport, namely stretching of fluid elements by a factor of 2 in the xy -plane to preserve cross-sectional area, and the Poiseuille distribution of \mathcal{T} (scaled such that the minimum advection time is unity) reflects the no-slip boundary conditions. Transport in a pore merge element is quantified by the inverse spatial map \mathcal{M}^{-1} , and the spatial residence time distribution is given by the composition $\mathcal{T} \circ \mathcal{M}^{-1}$. Although the advective maps $\mathcal{M}, \mathcal{M}^{-1}$ are not area-preserving, \mathcal{M} and \mathcal{M}^{-1} are implicitly volume-preserving when the fluid velocity in the z -direction is accounted for. Concatenation of a pore branch and merger results in area preservation and zero net fluid deformation, as reflected $\mathcal{M}^{-1} \circ \mathcal{M} = I$, where I is the identity operator.

Pore branches and mergers at arbitrary relative orientation θ in the xy -plane break this symmetry and do not result in such degeneracy. Rather, the rotation operator

$$R(\theta) : \{x, y\} \mapsto \{x \cos \theta + y \sin \theta, y \cos \theta - x \sin \theta\}, \quad (3.6)$$

coupled with the pore branch \mathcal{M} and merge \mathcal{M}^{-1} maps define transport in pore branches and mergers at arbitrary angles

$$\mathcal{S}(\theta) = R(\theta) \circ \mathcal{M} \circ R(-\theta), \quad (3.7)$$

$$\mathcal{S}^{-1}(\theta) = R(\theta) \circ \mathcal{M}^{-1} \circ R(-\theta), \quad (3.8)$$

where $\mathcal{S}(\theta_1) \circ \mathcal{S}(\theta_2) \neq I$ for $\theta_1 \neq \theta_2$. Coupled with the residence time distribution \mathcal{T} , the composite maps $\mathcal{S}, \mathcal{S}^{-1}$ quantify advective transport through the 3D porous network, and the position and residence time of fluid particles can be rapidly propagated via these approximate maps. The distribution of alignment angles θ dictates fluid stretching within the network, where the sequence of angles $\theta_1, \theta_2, \dots$ for a particular trajectory can impart either chaotic or non-chaotic advection (Lester *et al.* 2013), and the associated infinite-time Lyapunov exponent spans $\lambda_\infty \in [0, \ln 2]$. Conversely, random media with θ uniformly distributed as a Markov process generates globally chaotic dynamics which are typically weaker than that of ordered media.

This basic pore network model has been used (Lester *et al.* 2013, 2014) to study the impact of Lagrangian chaos upon dispersion in porous media, i.e. the spatial spreading of transport particles. Here, we investigate its impact on mixing properties, i.e. the distribution and temporal dynamics of concentration statistics by explicitly coupling fluid deformation with molecular diffusion. Figure 4 (b) illustrates the macroscopic evolution of a dye trace simulation propagated by the composite maps $\mathcal{S}, \mathcal{S}^{-1}$ following a single pore through a realization of the random network. The lower right sub-figure in Figure 4 (b) illustrates the creation of fine-scale structure via chaotic advection within the

pore-scale (from an initially segregated distribution of half blue/half red points across all pores), and the upper left subfigure shows evolution of the residence time distribution evolved via the composite temporal maps $\mathcal{S} \circ \mathcal{T}$, $\mathcal{S}^{-1} \circ \mathcal{T}$. Note there is no evidence of folding of fluid elements in the xy -plane as folding occurs around stagnation points as fluid elements are advected downstream in the z -direction.

4. Stretching and Compression in 3D Porous Networks

4.1. Stretching and Compression in 3D Ordered Networks

To calculate transport, mixing and dispersion with the random 3D porous network model, we first consider the deformation of a continuously injected 2D material filament under a mean flow in the z -direction as it propagates over pore branches and mergers through the network. To determine the evolution of this 2D material filament throughout in 3D random network, it shall prove convenient to consider this steady 2D filament as an evolving 1D material line in the mapping-planes, the constituent points of which are projected via the advective maps $\mathcal{S}(\theta)$, $\mathcal{S}(\theta)^{-1}$.

Whilst fluid stretching does occur in the z -direction (due to both deformation in the parabolic flow field and iterated stretching and compression over pore branches and mergers), the impact upon mixing is considered negligible due to alignment of the continuously injected 2D filament with the mean flow direction. Hence the gross impact of chaotic advection upon dispersion and mixing under steady-state conditions is to accelerate mixing transverse to the mean flow direction z . As such, only the stretching dynamics in the xy -plane are required to quantify mixing under steady flow conditions.

As the advective map \mathcal{M} represents the flow (in the dynamical systems sense) of fluid particles from the inlet to outlet pores, the 2D fluid deformation gradient tensor \mathbf{F}_{2D} over a pore branch is given by the gradient which may be linearised as

$$\mathbf{F}_{2D} = \frac{\partial \mathcal{M}_i}{\partial x_j} = \begin{pmatrix} 1 & \pm \frac{x}{\sqrt{1-x^2}} \\ 0 & 2 \end{pmatrix} \approx \begin{pmatrix} 1 & 0 \\ 0 & 2 \end{pmatrix}, \quad (4.1)$$

and likewise fluid deformation over a pore merger is given by \mathbf{F}_{2D}^{-1} . CFD simulations of Stokes flow through the branch element Ω shows that this linearisation well approximates fluid deformation in the branch and merge elements. The gross action of the pore branch is to stretch fluid elements by a factor of 2 in the y -direction, and simultaneously contract elements by a factor of $\frac{1}{2}$ in the z -direction (not reflected in \mathbf{F}_{2D} , whilst conversely the pore merger contracts fluid elements by a factor of $\frac{1}{2}$ in the y -direction and stretches by a factor of 2 in the z -direction. Similar to the advective maps \mathcal{M} , \mathcal{M}^{-1} , the concatenated branch and merge deformation tensors generate zero net stretching ($\mathbf{F}_{2D} \cdot \mathbf{F}_{2D}^{-1} = \mathbf{1}$), but when reoriented, concatenation of these tensors can generate persistent fluid stretching.

To quantify stretching and compression in an ordered 3D porous network, we consider the reoriented deformation tensors

$$\mathbf{S}_s = \mathbf{R}(\theta_s) \cdot \mathbf{F}_{2D} \cdot \mathbf{R}^{-1}(\theta_s), \quad (4.2a)$$

$$\mathbf{S}_c = \mathbf{R}(\theta_c) \cdot \mathbf{F}_{2D}^{-1} \cdot \mathbf{R}^{-1}(\theta_c), \quad (4.2b)$$

where $\mathbf{R}(\theta)$ is the rotation matrix associated with reorientation through angle θ in the xy -plane. Fluid deformation over a coupled pore branch/merge element (couplet) is then

$$\begin{aligned} \mathbf{S} &= \mathbf{S}_s \cdot \mathbf{S}_c, \\ &= \mathbf{R}(\theta_s) \cdot \mathbf{F}_{2D} \cdot \mathbf{R}(\Delta) \cdot \mathbf{F}_{2D}^{-1} \cdot \mathbf{R}^{-1}(\Delta) \cdot \mathbf{R}^{-1}(\theta_s), \\ &= \mathbf{R}(\theta_s) \cdot \mathbf{D}(\Delta) \cdot \mathbf{R}^{-1}(\theta_s), \end{aligned} \quad (4.3)$$

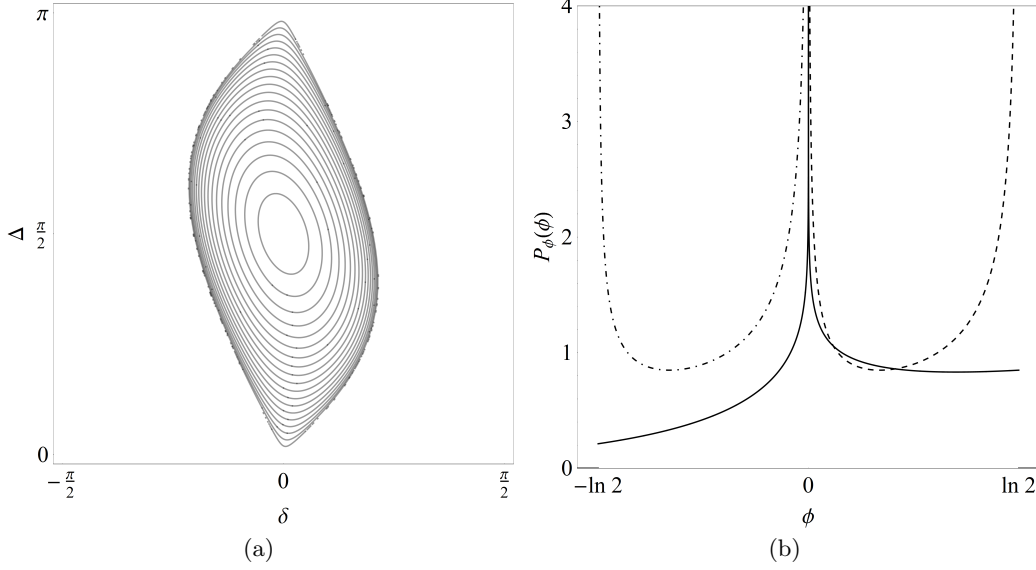


FIGURE 5. (a) Contour plot of the distribution of logarithmic stretching rates $\lambda(\delta, \Delta)$ in ordered 3D networks as a function of the orientation angles δ, Δ , between and within pore couplets. The stretching rate λ varies between $\lambda = 0$ for $|\zeta| \leq 1$ and the theoretical maximum for continuous systems $\lambda = \ln 2$ for $\zeta = \frac{5}{4}$ at $\Delta = \pi/2, \delta = 0$. (b) PDF of logarithmic stretching rates $P_\phi(\phi)$ (solid), $P_{\phi_s}(\phi_s)$ (dashed) and $P_{\phi_c}(\phi_c)$ (dot-dashed) in random 3D networks. Note $P_\phi(\phi)$ is strongly peaked but asymmetric around $\phi = 0$.

where $\Delta := \theta_s - \theta_c$. The logarithm of the eigenvalues of $\mathbf{S}, \mathbf{D}(\Delta)$ are the stretching rates over a couplet

$$\lambda_{b,m} = \pm \ln(\zeta + \sqrt{\zeta^2 - 1}), \quad (4.4)$$

where $\zeta = \frac{9}{8} - 18 \cos 2\Delta$. For pore branches and mergers which are parallel ($\Delta = n\pi, n = 0, 1, 2, \dots$), there is no net stretching ($\zeta = 0$), whereas orthogonally oriented elements ($\Delta = \pi/2 + n\pi, n = 0, 1, 2, \dots$) generate maximum stretching $\lambda_c = \ln 2$ akin to the baker's map. Net fluid deformation over a series of n concatenated couplets is then given by the series

$$\begin{aligned} \mathbf{A}_n &= \mathbf{R}(\theta_n) \cdot \mathbf{D}(\Delta_n) \cdot \mathbf{R}^{-1}(\theta_n) \cdots \mathbf{R}(\theta_1) \cdot \mathbf{D}(\Delta_1) \cdot \mathbf{R}^{-1}(\theta_1), \\ &= \mathbf{R}(\theta_n) \cdot \left(\prod_{j=1}^n \mathbf{L}(\delta_j, \Delta_j) \right) \cdot \mathbf{R}^{-1}(\theta_n), \end{aligned} \quad (4.5)$$

where $\mathbf{L}(\delta, \Delta) := \mathbf{R}(\delta) \cdot \mathbf{D}(\Delta)$, $\delta_j = \theta_{j+1} - \theta_j$ for $j = 1 : n-1$ and $\delta_n = \theta_1 - \theta_n$. As such, the deformation tensor $\mathbf{L}(\delta, \Delta)$ quantifies fluid deformation over a series of connected pore couplets, and net fluid deformation depends strongly upon the series of angles Δ_j within couplets and the series of relative orientation δ_j between couplets.

For ordered media which consists of a fixed δ and Δ , net fluid deformation is quantified by the infinite-time Lyapunov exponent λ given by the logarithm of the eigenvalues of the deformation tensor $\mathbf{L}(\delta, \Delta)$

$$\lambda(\delta, \Delta) = \pm \ln |\zeta + \sqrt{\zeta^2 - 1}|, \quad (4.6)$$

where $\zeta = \frac{9}{8} \cos \delta - \frac{1}{8} \cos(2\Delta + \delta)$. As shown in Figure 5 (a), zero net deformation occurs for $|\zeta| \leq 1$, whilst maximum deformation ($\lambda = \ln 2$) occurs for $\Delta = (n + \frac{1}{2})\pi, \delta = n\pi$.

Note that zero net stretching is possible even if pore branches and mergers are oriented transversely ($\Delta = (n + \frac{1}{2})\pi$); whilst maximum fluid stretching occurs within a couplet, if a neighbouring couplets are oriented transversely ($\delta = (n + \frac{1}{2})\pi$), then the transverse stretching in the next couplet cancels the net deformation. Hence ordered 3D porous networks represent extreme cases with respect to fluid stretching and deformation; whilst a large class ($|\zeta| \leq 1$) of ordered media do not exhibit chaotic advection ($\lambda = 0$), certain networks exhibit the maximum theoretic stretching ($\lambda = \ln 2$) for continuous systems.

The stretching rate $\lambda(\delta, \Delta)$ quantifies stretching of the 2D material filament as it propagates through the 3D network in the that the length l of the filament cross section in the xy -plane grows with longitudinal pore number n or distance z as

$$l(z) = l_0 \exp(\lambda(\delta, \Delta)n) = l_0 \exp\left(\lambda(\delta, \Delta)\frac{z}{\ell}\right), \quad (4.7)$$

where l_0 is the initial length of the filament cross section. In the presence of chaotic advection where $\lambda > 0$, unbounded growth of the filament cross section is accommodated by striated packing within pores as per Figure 4.

4.2. Stretching and Compression in 3D Random Networks

In contrast to ordered 3D networks, the orientation angle θ between pore elements in the model random 3D network follows a Markov process, and so the average stretching rate λ_∞ (Lyapunov exponent) is

$$\lambda_\infty = \frac{1}{\pi^2} \int_{-\pi/2}^{\pi/2} d\delta \int_0^\pi d\Delta \lambda(\delta, \Delta) \approx 0.1178, \quad (4.8)$$

which closely matches the numerically computed asymptotic stretching rate calculated from the advective maps $\mathcal{S}(\theta)$, $\mathcal{S}(\theta)$ for random θ (Lester *et al.* 2013).

We consider evolution of an infinitesimal element within the 1D material line represented by the vector \mathbf{l} , where \mathbf{l} evolves with pore number n over pore branch and merge elements respectively as

$$\mathbf{l}_{2n+1} = \mathbf{R}(\theta_s) \cdot \mathbf{F}_{2D} \cdot \mathbf{R}^{-1}(\theta_s) \cdot \mathbf{l}_{2n}, \quad (4.9a)$$

$$\mathbf{l}_{2n+2} = \mathbf{R}(\theta_c) \cdot \mathbf{F}_{2D}^{-1} \cdot \mathbf{R}^{-1}(\theta_c) \cdot \mathbf{l}_{2n+1}, \quad (4.9b)$$

where θ_s , θ_c are the orientation angles of the pore branch, merger with respect to the y -direction as per Figure 2. The length $l = |\mathbf{l}|$ of the line element then evolves via the two-step process

$$l_{n+1} = l_n \rho_s(\varphi_n), \quad (4.10a)$$

$$l_{n+2} = l_{n+1} \rho_c(\varphi_{n+1}), \quad (4.10b)$$

where φ_n are the orientation angles of the pore branch or merger with respect to the line element and ρ_s , ρ_c respectively are the relative elongation due to stretching and compression within a pore branch and merger:

$$\rho_s(\varphi_s) = \sqrt{1 + 3 \cos^2 \varphi_s}, \quad (4.11a)$$

$$\rho_c(\varphi_c) = \frac{1}{2} \sqrt{4 - 3 \cos^2 \varphi_c}. \quad (4.11b)$$

For random media, the pore branches and mergers are randomly oriented such that φ_s , φ_c are uniformly distributed over $\theta \in [-\pi, \pi]$. As such, it is not necessary to consider the orientation of the material line as φ_s , φ_c are also uniformly distributed over $[-\pi, \pi]$, and so the mean relative stretching λ_s and compression λ_c within a pore branch and merger

are

$$\lambda_s = \frac{1}{2\pi} \int_{-\pi}^{\pi} d\varphi_s \ln[\rho_s(\varphi_s)] \approx 0.405465, \quad (4.12a)$$

$$\lambda_c = \frac{1}{2\pi} \int_{-\pi}^{\pi} d\varphi_c \ln[\rho_c(\varphi_c)] \approx -0.287682, \quad (4.12b)$$

where the sum of these stretching rates recovers the infinite-time Lyapunov exponent $\lambda_s + \lambda_c = \lambda_\infty \approx 0.11783$. The full distribution of stretching rates can also be derived from (4.11) as

$$P_{\rho_s}(\rho_s) = \frac{4}{\pi \sqrt{\rho_s^2 - 1} \sqrt{4 - \rho_s^2}}, \quad \rho_s \in [1, 2], \quad (4.13)$$

$$P_{\rho_c}(\rho_c) = \frac{4}{\pi \sqrt{1 - \rho_c^2} \sqrt{4\rho_c^2 - 1}}, \quad \rho_c \in [\frac{1}{2}, 1], \quad (4.14)$$

and the total stretch $\rho := \rho_s \rho_c$ over a couplet is distributed as

$$\begin{aligned} P_\rho(\rho) &= \int_{\frac{1}{2}}^1 d\rho'_c \int_1^2 d\rho'_s P_{\rho_s}(\rho'_s) P_{\rho_c}(\rho'_c) \delta(\rho - \rho'_c \rho'_s), \\ &= \frac{4}{\pi^2} \left| \frac{\rho}{\rho^2 - 1} \right| K \left(1 - \frac{9\rho^2}{4\rho^2 - 4} \right), \quad \rho \in [\frac{1}{2}, 2], \end{aligned} \quad (4.15)$$

where K is the complete elliptic integral of the first kind. To derive the total stretching over many pore couplets, it is convenient to consider evolution of the logarithmic length $s := \ln l$ of a line element, where s evolves over a couplet via the one-step additive process

$$s_{n+2} = s_n + \phi_s + \phi_c = s_n + \phi, \quad (4.16)$$

where $\phi_s = \ln \rho_s$, $\phi_c = \ln \rho_c$, and $\phi = \phi_s + \phi_c = \ln \rho$ are distributed as

$$P_\phi(\phi) = \exp(\phi) P_\rho(\exp \phi), \quad \phi \in [-\ln 2, \ln 2], \quad (4.17)$$

$$P_{\phi_s}(\phi_s) = \exp(\phi_s) P_{\rho_s}(\exp \phi_s), \quad \phi_s \in [0, \ln 2], \quad (4.18)$$

$$P_{\phi_c}(\phi_c) = \exp(\phi_c) P_{\rho_c}(\exp \phi_c), \quad \phi_c \in [-\ln 2, 0], \quad (4.19)$$

Asymmetry of the stretching PDF $P_\phi(\phi)$ for random φ_s, φ_c leads to persistent fluid stretching as shown in Figure 5(b) and reflected by the Lyapunov exponent λ_∞ . This asymmetry arises from the asymmetry between the stretching and compression processes; within a pore branch stretching is enhanced as the material line rotates toward the maximum stretching direction, whilst compression is retarded in a pore merger due to rotation away from the contraction direction. Hence whilst transverse fluid stretching and compression are equally partitioned in random 3D networks, the asymmetry between stretching and compression generates persistent chaotic advection.

As both the mean (λ_∞) and the variance ($\sigma^2 \approx 0.11436$) of $P_\phi(\phi)$ are bounded, then the sum of the stretching increments ϕ converges with n toward a Gaussian distribution via the central limit theorem, such that s_n is approximately distributed as

$$P_{s_n}(s) \approx \frac{1}{\sigma \sqrt{n\pi}} \exp \left[-\frac{(s - s_0 - \frac{n}{2} \lambda_\infty)^2}{n\sigma^2} \right], \quad (4.20)$$

where the initial element length $s_0 = \ln l_0$. Thus, the PDF of the non-dimensional strip elongation $\rho_n = l_n/l_0$ is given by the lognormal distribution

$$\hat{p}_\rho(\rho, n) = \frac{1}{\rho \sqrt{\pi n \sigma^2}} \exp \left[-\frac{(\ln \rho - n\lambda_\infty/2)^2}{n\sigma^2} \right], \quad (4.21)$$

which captures convergence of the distribution of finite Lyapunov exponents $\lambda_n = s_n/n$ toward λ_∞ as shown in (Lester *et al.* 2013).

As 2D material filaments flow through pore branches and mergers in random 3D porous networks, they undergo a series of punctuated stretching and compression events around stagnation points which leads to net exponential stretching transverse to the mean flow direction. The length of material elements transverse to the mean flow direction are distributed log-normally, and the mean and variance respectively grow with n as $n\lambda_\infty/2$ and $n\sigma^2/2$.

Notice that the PDF (4.21) quantifies the point-wise elongation statistics. When sampling the lamella elongation in space, however, the sampling rate is proportional to the length of the lamella. This is of particular importance because concentration statistics of the heterogeneous mixture are determined by spatial sampling across the lamellae. The elongation PDF weighted by the lamellae length, $p_\rho(\rho, n) \propto \rho \hat{p}_\rho(\rho, n)$, is given by

$$p_\rho(\rho, n) = \frac{1}{\rho \sqrt{2\pi\sigma_{\ln\rho}^2}} \exp \left[-\frac{(\ln \rho - \mu_{\ln\rho})^2}{2\sigma_{\ln\rho}^2} \right], \quad (4.22)$$

where we defined

$$\mu_{\ln\rho} = n(\lambda_\infty + \sigma^2)/2, \quad \sigma_{\ln\rho}^2 = \sigma^2 n/2. \quad (4.23)$$

For simplicity of notation in the following we set $\Lambda_\infty = \lambda_\infty + \sigma^2$. To study the impact of pore-scale chaotic dynamics on fluid mixing and transport, we compare several different types of open networks, from random 3D networks ($\lambda = \lambda_\infty$), ordered 3D networks with maximum stretching ($\lambda = \ln 2$), and 2D networks ($\lambda = 0$) which have the same dynamics as ordered 3D networks with zero stretching.

5. Stretching Continuous Time Random Walk

The stretching dynamics for ordered and random media developed above provide inputs for the evolution of mixing in porous networks. We propose to describe the deformation process via a stretching Continuous Time Random Walk (CTRW), whereby fluid elements undergo a series of punctuated stretching and folding events as they propagate through the topologically complex pore network. CTRW models have been previously developed for modeling dispersion processes, based on the observation that Lagrangian velocities in porous media tend to be non-Markovian in time but Markovian in space (Le Borgne *et al.* 2008a; de Anna *et al.* 2013). This property is a consequence of the nature of the considered velocity fluctuations, which are created by solid structures that can often be described by a characteristic length scale (e.g. typical grain size or permeability field correlation length). As low Lagrangian velocities are maintained over this characteristic length scale, they are likely to persist over large time scales. Spatial Markov models formalized in the CTRW framework capture this broad transit time distribution (Le Borgne *et al.* 2008b; Bijeljic *et al.* 2011). Similarly to advective motions, fluid stretching events are likely to persist over a finite correlation scale, which is the pore length in the present study, and will therefore occur in broadly distributed random times. This is the basis for the proposed stretching CTRW model.

As fluid mixing involves the interplay of advection and diffusion, and the diffusion process is dependent upon the advection time over pore branches and mergers, it is necessary to extend the two-step stretching process (4.10) to include quantification of

advection as a two-step CTRW:

$$l_{2n+1} = l_{2n}\rho_s(\varphi_n), \quad t_{2n+1} = t_{2n} + \Delta t_{2n}, \quad (5.1a)$$

$$l_{2n+2} = l_{2n+1}\rho_c(\varphi_{2n+1}), \quad t_{2n+2} = t_{2n+1} + \Delta t_{2n+1}, \quad (5.1b)$$

where the time increment Δt_n represents the advection time between pore elements. The stretching CTRW (5.1) consists of punctuated random stretching ρ_s and compression ρ_c processes which occur within each pore. The duration of the stretching and compression events is distributed as $\psi(\Delta t)$. Thus, the stretching CTRW quantifies the elongation of a material segment at subsequent downstream positions z_n through l_n , and the deformation time through the temporal random walk t_n . The deformation rates during a stretching or compression transition are constant and given by

$$\gamma_n = \frac{\ln[\rho_s(\varphi_n)]}{\Delta t_n}, \quad \gamma_{n+1} = \frac{\ln[\rho_c(\varphi_{n+1})]}{\Delta t_{n+1}}, \quad (5.2)$$

and so, we obtain for the strip length $l(t)$

$$l(t) = l_{n_t} \exp[\gamma_{n_t}(t - t_{n_t})], \quad (5.3)$$

where the renewal process $n_t = \sup(n | t_n \leq t)$ measures the number of steps needed to arrive at time t .

From the temporal map \mathcal{T} , the advection of fluid particles through a pore branch or merger is well-approximated by the Poiseuille flow

$$v(r) = v_0 \left(1 - \frac{r^2}{R}\right) \quad (5.4)$$

with v_0 the maximum velocity and R the pore radius. Thus, in the absence of diffusion, the transition time over a pore branch element at radius r is given by $\Delta t(r) = \ell/v(r)$ with ℓ the length of the pore branch element. Due to the ergodicity of chaotic orbits, particles sample the whole cross-section with equal probability, and so the transition time distribution is given by the Pareto distribution

$$\psi(\Delta t) = \frac{1}{\Delta t_a} \left(\frac{\Delta t}{\Delta t_a} \right)^{-2}, \quad \Delta t \geq \Delta t_a. \quad (5.5)$$

where $\Delta t_a = \ell/v_0$. For porous media which are more complex than the model pore network under consideration here, pore velocities are often found to align according to exponential or stretched exponential distributions (Moroni & Cushman 2001; Kang *et al.* 2014; Siena *et al.* 2014; Holzner *et al.* 2015). The corresponding transit times shows a similar long time behavior as (5.5).

Derivation of the distribution of average stretch ρ over a couplet allows the two step CTRW (5.1) to be replaced with the one-step CTRW

$$s_{2n+2} = s_{2n} + \phi_{2n}, \quad t_{n+2} = t_{2n} + \Delta t_{2n} + \Delta t_{2n+1}. \quad (5.6)$$

Note that the stretching rate for this one-step CTRW is not uniform over a couplet (given by the time increment $\Delta t_{2n} + \Delta t_{2n+1}$), but rather is highly oscillatory due to the mean stretching rate λ_s, λ_c over a pore branch or merger respectively. Whilst such oscillations do not impact the overall stretching rate λ_∞ , they may have significant implications for molecular diffusion as oscillatory stretching can leave a diffusive signature over the couplet. We shall return to this issue in §6.

Whilst the length-weighted distribution of material lengths $\rho_n = l_0 \exp s_n$ given by the PDF (4.22) characterizes material deformation over a couplet under action of the 2D

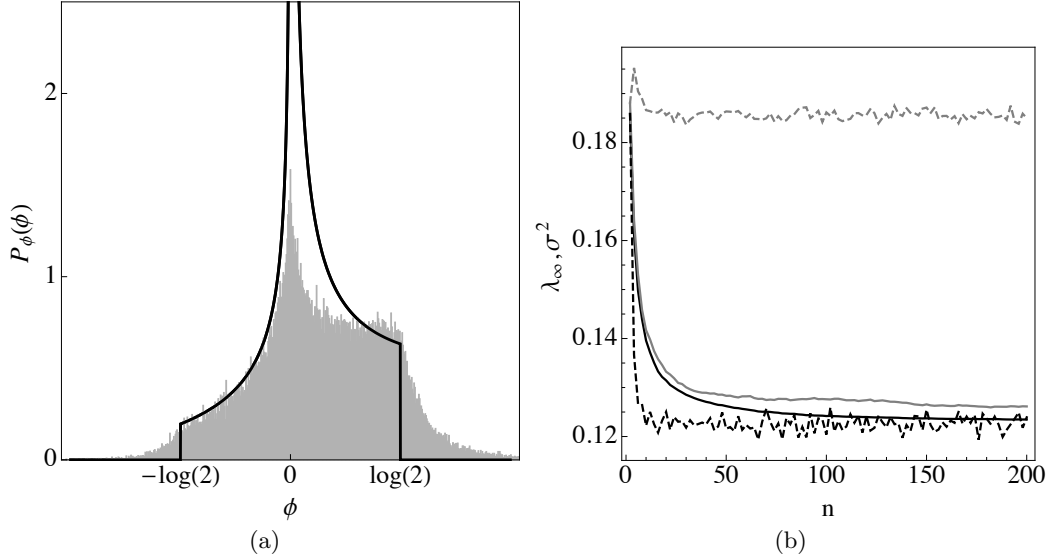


FIGURE 6. (a) Comparison of the PDFs of logarithmic stretching $P_\phi(\phi)$ over a couplet computed from the nonlinear advective map \mathcal{M} (solid gray) or derived the linearised deformation tensor \mathbf{F}_{2D} (black line). (b) Evolution of the mean λ_∞ (black, solid) and variance σ^2 (gray, solid) of material deformation with the number of pores n , and convergence of the increment of the mean $\langle \phi_{n+1} \rangle - \langle \phi_n \rangle$ (black, dashed) and variance $\langle (\phi_{n+1} - \langle \phi_{n+1} \rangle)^2 \rangle - \langle (\phi_n - \langle \phi_n \rangle)^2 \rangle$ (gray, dashed), respectively reflecting anti-correlation and non-stationarity of the advective map \mathcal{M} .

deformation tensors $\mathbf{F}_{2D}, \mathbf{F}_{2D}^{-1}$, these operators do not capture the full deformation due to linearisation of the map \mathcal{M} . The nonlinear shear deformation in \mathcal{M} generates additional deformation as reflected by the comparison of stretching rates over a couplet between the advective map \mathcal{M} and linearised deformation tensor \mathbf{F}_{2D} in Figure 6(a). Deformation due to nonlinear shear extends the range of stretching beyond the bounds $\rho \in [1/2, 2]$ and increases the asymmetry of the stretching process, increasing both the variance and mean of the stretching distribution over a couplet to $\sigma^2 \approx 0.1277$ $\lambda_\infty \approx 0.124$ respectively.

Furthermore, the stretching process over a couplet under \mathcal{M} is both non-stationary and anti-correlated due to preferential alignment of initially random oriented material elements with the pore boundary as they undergo stretching. This is purely a geometric effect in that highly striated fluid elements must preferentially align tangentially with the pore boundary to allow packing within a finite domain. As the stretching process under \mathcal{M} rapidly converges (after 20 pores) to a stationary process, the increment of the mean $\langle \phi_{n+1} \rangle - \langle \phi_n \rangle$ and variance $\langle (\phi_{n+1} - \langle \phi_{n+1} \rangle)^2 \rangle - \langle (\phi_n - \langle \phi_n \rangle)^2 \rangle$ quickly converge as per Figure 6(b). Conversely, anti-correlation causes these moments to converge more slowly toward the asymptotic values $\lambda_\infty \approx 0.12770$, $\sigma^2 \approx 0.12366$. Rather than develop a stochastic model which fully captures non-stationarity and anti-correlation, we approximate this process by using the uncorrelated and stationary one-step stretching CTRW (5.6), where the increment ϕ is from the distribution shown in Figure 6(a) with mean and variance given by these asymptotic values. Figure 7 shows that the lognormal form (4.22) parameterized by the asymptotic values of $\lambda_\infty \approx 0.12770$, $\sigma^2 \approx 0.12366$ compares very well with PDFs of $\ln \rho$ from direct numerical calculation.

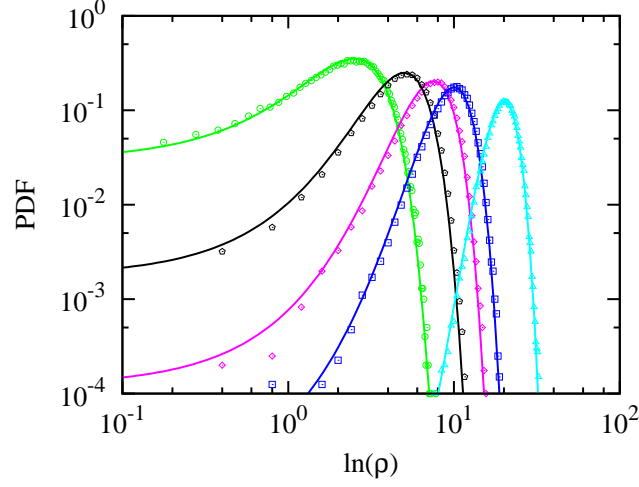


FIGURE 7. Comparison of the lognormal form (4.22) of the PDF of $\ln \rho$ (lines) to the PDFs obtained numerically from the one-step CTRW model (5.6) for (circles) $n = 20$, (pentagons) $n = 40$, (diamonds) $n = 60$, (squares) $n = 80$, (triangles) $n = 160$.

6. Scalar Mixing and Fluid Stretching CTRW

To describe the interplay of fluid stretching and molecular diffusion in the generation of scalar mixing in the pore space we employ a lamellar mixing model (Ranz 1979; Duplat & Villiermaux 2008; Le Borgne *et al.* 2015), where fluid stretching is quantified by the CTRW model developed in §5. Under exponential fluid stretching, an evolving concentration field conforms to a highly striated lamellar structure, where these lamellae align with the dominant stretching direction(s) and are simultaneously stretched longitudinally and compressed transversely.

We define a single lamella in the 3D pore space as the 2D invariant manifold which arises from the continuous injection of solute into a single pore in the inlet plane ($z = n = 0$). For simplicity we consider the injected solute concentration to be distributed as a concentration strip of length l_0 with a transverse Gaussian profile of maximum concentration c_0 and variance σ_0^2 , and the 2D lamella sheet (a material surface) evolves via the downstream advection of the 1D ridge of the injected concentration distribution. Hence the 2D lamella sheet acts as a backbone for the longitudinally evolving concentration field c , and this 2D surface is deformed and stretched as it evolves under advection throughout the pore-space, branching into multiple pores (as per Figure 4) but remaining smooth and continuous.

The ensemble of all 2D lamellae arising from injection across all injection pores are homogeneously distributed throughout the pore network and so lamellae from different injection pores coexist within a given pore (as per Figure 4) with spacing that decays as the exponential stretching rate in the longitudinal direction, but do not intersect due to their invariant nature. Conversely, the 3D concentration distributions associated with 2D lamellae may overlap, resulting in the eventual coalescence of lamellae in the longitudinal direction.

The steady 3D concentration field $c(\mathbf{x})$ local to an individual 2D lamella sheet arises from the interplay of fluid deformation and molecular diffusion local to this structure, and satisfies the steady advection diffusion equation (ADE)

$$-\mathbf{v}(\mathbf{x}) \cdot \nabla c(\mathbf{x}) + D_m \nabla^2 c(\mathbf{x}) = 0, \quad (6.1)$$

subject to the zero-flux condition $\nabla c(\mathbf{x}) \cdot \mathbf{n}|_{\partial\mathcal{D}} = 0$, where $\mathbf{v}(\mathbf{x})$ is the 3D velocity field, D_m molecular diffusivity, and \mathbf{n} is the outward normal from the fluid domain \mathcal{D} . Under the assumption that the spatial concentration gradients are small in the z -direction (corresponding to minimal curvature of the lamella in this direction), we ignore longitudinal diffusion and pose the steady 3D ADE (6.1) as an equivalent unsteady 2D ADE in the xy -plane

$$\frac{\partial c}{\partial t} = v_z \frac{\partial c}{\partial z} = -\mathbf{v}_\perp(x, y, t) \cdot \nabla_\perp c(x, y, t) + D_m \nabla_\perp^2 c(x, y, t), \quad (6.2)$$

where v_z is the z -component of $\mathbf{v}(\mathbf{x})$, \mathbf{v}_\perp and ∇_\perp denote the xy -components of velocity and gradient operator respectively. The z -coordinate is also parameterised in terms of the Lagrangian travel time $t = t(z)$ along a given fluid particle trajectory as

$$t(z) = \int_0^z dz' \frac{1}{v_z(z')}. \quad (6.3)$$

Whilst the travel time $t(z_0)$ for fixed $z = z_0$ also varies over the xy -plane, (6.2) provides a convenient basis for solution of the concentration field based upon a CTRW for the advection time and deformation history of fluid elements.

The lamellar mixing model is based upon posing (6.2) in terms of the material coordinates $\{\eta, \zeta\}$ in the xy -plane, where ζ is the coordinate along the lamella, and η is the transverse coordinate, hence $c(x, y, t) \mapsto c(\eta, \zeta, t)$. Under exponential fluid stretching, concentration gradients along the lamella (∂_ζ) decay exponentially whilst the gradients normal to the lamella (∂_η) are maintained, and so (6.2) simplifies to the 1D lamellar transport equation (Ranz 1979; Duplat & Villiermaux 2008; Villiermaux 2012; Le Borgne *et al.* 2013)

$$\frac{\partial}{\partial t} c(\eta, \zeta, t) = \gamma(t, \zeta) \eta \frac{\partial}{\partial \eta} c(\eta, \zeta, t) + D_m \frac{\partial^2}{\partial \eta^2} c(\eta, \zeta, t), \quad (6.4)$$

where the stretching rate $\gamma(t, \zeta) \equiv \partial_\zeta v_\zeta = -\partial_\eta v_\eta$ arises from a first order expansion of the η -component of the velocity field as

$$\begin{aligned} v_\eta(\eta, \zeta, t) &= v_\eta(0, \zeta, t) + \eta \frac{\partial}{\partial \eta} v_\eta(\eta, \zeta, t) + \dots, \\ &= v_\eta(0, \zeta, t) - \gamma(t, \zeta) \eta + \dots, \end{aligned} \quad (6.5)$$

under the change of coordinates to the material frame. The stretching rate $\gamma(t, \zeta)$ can be expressed in terms of the lamella elongation in the xy -plane $l(t, \zeta)$ as

$$\gamma(t, \zeta) \equiv \frac{\partial v_\zeta}{\partial \zeta} = \frac{d \ln l(t, \zeta)}{dt}. \quad (6.6)$$

Note that the 1D nature of (6.4) renders it only valid up to the coalescence of lamellae in the pore-space. Whilst methods (Duplat & Villiermaux 2008; Villiermaux 2012; Le Borgne *et al.* 2013) exist to propagate the concentration field beyond coalescence and are readily applicable to this problem, they are beyond the scope of this present study. As such, (6.7) describes the evolution of the concentration field $c(\eta, \zeta, t)$ with Lagrangian time t associated with either a single 2D lamella sheet or multiple lamellae via superposition.

As a lamella injected at a given pore at the injection plane $z = n = 0$ is distributed over many pores as it is advected downstream, segments of the material coordinate ζ are likewise distributed over multiple pores. Whilst in principle this may complicate solution of the evolving concentration field, for the homogeneous injection protocol all pores at the injection plane $z = n = 0$ are seeded with the same initial condition, and so

the re-distribution of lamellar segments between pores does not impact the concentration distribution at a statistical level. Hence the ADE (6.4) describes the spatial concentration distribution of a series of lamellar segments in an arbitrary pore, irrespective of origin. Whilst this simplification no longer holds for inhomogeneous injection protocols such as point or line sources, results for the homogeneous injection protocol may be readily extended as demonstrated in §7.

Due to negligible transport in the ζ direction, (6.4) may also be posed with respect to a single material fluid element trajectory that represents an infinitesimal lamella element, and so describes evolution of the associated transverse concentration $c(\eta, t)$ profile as

$$\frac{\partial}{\partial t}c(\eta, t) = \gamma(t)\eta\frac{\partial}{\partial\eta}c(\eta, t) + D_m\frac{\partial^2}{\partial\eta^2}c(\eta, t). \quad (6.7)$$

This particle-based description of fluid mixing is now compatible with the CTRW stretching framework, which describes the advection and deformation of fluid elements through the pore network, in terms of the advection time and deformation history. As such, we do not seek to directly solve the evolution of an entire lamella, but rather solve the evolving concentration profile $c(\eta, t_n)$ over a representative ensemble of points which recovers the same statistics of the ensemble of all lamellae in the pore-space due to ergodicity.

If we consider fluid advection and stretching as stochastic processes, then for given z_n or n the advection time $t_n = t(z_n)$ is distributed randomly according to the waiting time distribution (5.5). Hence $c(\eta, t_n)$ is a random variable through its dependence on both the random advection time t_n and random deformation $\gamma_n = \gamma(t_n)$. Under the assumption of independent lamellae, the PDF of concentration at a cross-section at z_n is obtained by (i) sampling the concentration values across the lamella, and (ii) sampling between the lamellae. This interpretation allows the lamellar mixing equation (6.7) to describe evolution of the transverse concentration profile with advection time and stretching history of any part of any lamellae in the entire 3D porous network.

In order to quantify scalar mixing, we first solve for the concentration profile $c(\eta, t)$ across a lamella. The initial concentration distribution across the strip is assumed to follow the Gaussian profile

$$c(\eta, 0) = \frac{c_0}{\sqrt{2\pi\sigma_0^2}} \exp\left(-\frac{\eta^2}{(2\sigma_0^2)}\right), \quad (6.8)$$

such that the maximum initial concentration $c_m(0) = c_0/\sqrt{2\pi\sigma_0^2}$ scales inversely with the initial variance σ_0^2 , and the initial strip length is denoted l_0 . For simplicity of exposition we first consider the case where this initial length and concentration profile is uniform across all pores at the injection plane $z = 0$ across the entire network, and so the concentration distribution at a given longitudinal pore number n is uniform across all transverse pores. We then extend these results to the case of a continuously injected point-source plume (as shown in Figure 4(b)) in §7.

To solve (6.7), we define the reduced coordinate η_0 and operational time $\tau(t)$ (Ranz 1979) as

$$\eta_0(t) = \eta\rho(t), \quad \tau(t) = \int_0^t dt' \rho(t')^2, \quad (6.9)$$

where $\rho(t) = l(t)/l(0)$. This is equivalent to a transformation into the characteristic

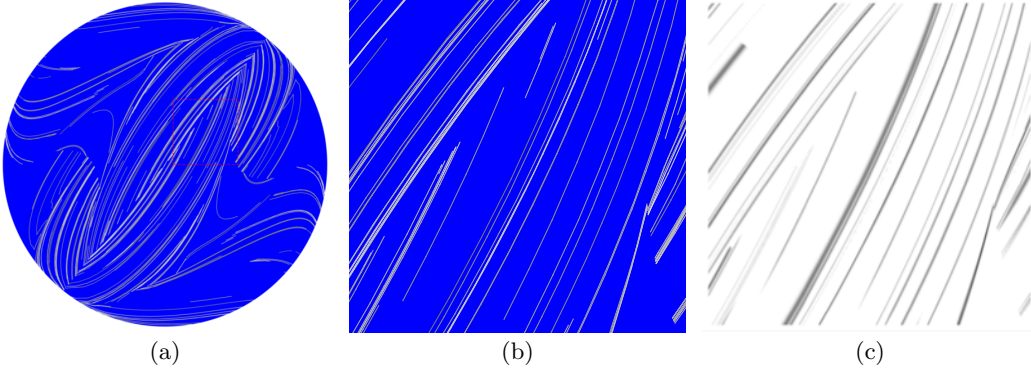


FIGURE 8. (a) Typical distribution of the logarithm of operational time $\ln \tau$ (black, $\ln \tau = 50$, white $\ln \tau = 5$) representing the backbone of the lamellar concentration field, with detail (dashed box) shown in (b). The associated scalar field $c(\mathbf{x})$ for $Pe = 10^8$ shown in (c) is calculated via the diffusive strip method (Meunier & Villiermaux 2010).

system of (6.7). Using this transformation, (6.7) simplifies to the diffusion equation

$$\frac{\partial g(\eta_0, \tau)}{\partial \tau} = D_m \frac{\partial^2 g(\eta_0, \tau)}{\partial \eta_0^2}, \quad (6.10)$$

whose solution for the Gaussian initial condition (6.8) is given by $g(\eta_0, \tau) = \exp[-\eta_0^2/2(\sigma_0^2 + 2D_m\tau)]/\sqrt{2\pi(\sigma_0^2 + 2D_m\tau)}$. Hence the concentration profile $c(\eta, t) = g[\eta_0(t), \tau(t)]$ across the strip is

$$c(\eta, t) = \frac{c_0}{\sqrt{2\pi[\sigma_0^2 + 2D_m\tau(t)]}} \exp\left[-\frac{\eta^2 \rho(t)^2}{2\sigma_0^2 + 4D_m\tau(t)}\right], \quad (6.11)$$

and so the transverse concentration profile is completely determined by the total stretch $\rho(t)$ which acts to stretch and narrow the lamellae and the stretching history as quantified by $\tau(t)$ which acts to broaden and dilute the lamellae. As $\tau(t)$ depends explicitly upon the entire stretching history, the stretching oscillations in the two-step process (5.1) over a couplet are captured by $\tau(t)$, and so must be appropriately quantified in the implementation of the one-step CTRW (5.6). The maximum concentration $c_m(t) = c(0, t)$ is now given by

$$c_m(t) = \frac{c_0}{\sqrt{2\pi[\sigma_0^2 + 2D_m\tau(t)]}}. \quad (6.12)$$

These results form the basis of the diffusive strip method (Meunier & Villiermaux 2010) which facilitates efficient solution of the 1D lamellar ADE (6.7) based upon the advection of fluid particles across a very broad range of Pe . We employ this method in conjunction with the advective \mathcal{M} and temporal \mathcal{T} maps over a pore couplet to rapidly simulate stretching of a 2D material filament within the 3D pore-space, and diffusion is calculated as a post-processing step for various Pe via (6.11) given determination of the distribution of ρ and τ along the strip from the stretching history. This method is capable of accurately capturing stretching, diffusion and coalescence of the scalar field up to $n \sim 100$ pores, beyond which exponential growth of the lamellar structure (and the associated number of representative points) is too large for feasible computation. A typical distribution of the operational time $\ln \tau$ over the cross-section of a 2D filament at longitudinal distance $n = 40$ pores is shown in Figure 8 along with the scalar field $c(\mathbf{x}, t_n)$ calculated at $Pe = 10^8$.

We non-dimensionalise (6.12) by introducing the variables

$$c'_m(t) = \frac{c_m(t)}{c_m(0)}, \quad t' = \frac{t}{\Delta t_a}, \quad \tau' = \frac{\tau}{\Delta t_a}, \quad (6.13)$$

with the characteristic advection time $\Delta t_a = \ell/v_0$; ℓ is the length of a pore and v_0 the mean pore velocity. In the following, we drop the primes for simplicity of notation. The maximum concentration is then

$$c_m(t) = \frac{1}{\sqrt{1 + \tau(t)/Pe}}, \quad (6.14)$$

where the Peclet number is defined as $Pe = \sigma_0^2 v_0 / (2D_m \ell)$. Dispersion across a material filament is dependent upon Pe and the entire stretching history encoded via the operational time $\tau(t)$.

The characterization of the concentration profile at location across the strip at the downstream position z_n is conditional on the quantification of the operational time $\tau(t_n)$ at time t_n . As expressed by (6.9), operational time depends on the deformation history through $\rho(t)$. In order to obtain a closed form expression for $\tau(t_n)$, we approximate the evolution of $\rho(t)$ between $t = 0$ and $t = t_n$ in terms of the average stretching rate $\Gamma_n = \ln(\rho_n)/t_n$ after n steps as

$$\rho(t) \approx \exp(\Gamma_n t). \quad (6.15)$$

From (6.15), the operational time $\tau(t_n)$ may then be approximated as

$$\tau_n \equiv \tau(t_n) \approx \frac{t_n \rho_n^2}{2 \ln(\rho_n)}. \quad (6.16)$$

This expression can be further simplified by noticing that the PDF (4.22) of $\ln(\rho_n)$ is Gaussian, with mean $n\Lambda_\infty/2$ and variance $n\sigma^2/2$. Thus, we may approximate the denominator in (6.16) by its mean value $2 \ln(\rho_n) \approx n\Lambda_\infty$,

$$\tau_n \approx \frac{t_n \rho_n^2}{n\Lambda_\infty}, \quad (6.17)$$

which becomes sharper with increasing n as shown in Figure 9(a). In essence, (6.17) solves the CTRW for molecular diffusion. Oscillations associated with the two-step stretching process (5.1) appear to play a minor role in the overall evolution of the operational time $\tau(t)$, hence τ_n is well-approximated by the one-step stretching process (5.6) characterized by the mean stretching rate Λ_∞ . Thus, whilst diffusion is in principle dependent upon the entire stretching history, the operational time τ_n which controls the diffusion process is predominantly governed by the arrival time t_n of the material strip at position z_n and the elongation ρ_n .

The PDF of $\xi_n = \ln(\tau_n) = \ln(t_n) + 2 \ln(\rho_n) - \ln(n\Lambda_\infty)$ can be estimated by approximating $\ln(t_n)$ by its average

$$\langle \ln t_n \rangle \approx \ln \left[\frac{n}{a} (\ln 2 + \gamma + b) + n (\ln n + 1 - \gamma) \right], \quad (6.18)$$

where γ is the Euler-Mascheroni constant and $a = 0.7413$ and $b = 0.0064$, see Appendix A. Since $\ln(\rho_n)$ is Gaussian distributed with the mean $n\Lambda_\infty/2$ and variance $n\sigma^2/2$, we obtain for the PDF of $\xi_n = \ln(\tau_n)$ the Gaussian

$$p_{\ln \tau}(\xi, n) = \frac{\exp \left(-\frac{[\xi - \mu_{\ln \tau}(n)]^2}{2\sigma_{\ln \tau}^2(n)} \right)}{\sqrt{2\pi\sigma_{\ln \tau}^2(n)}} \quad (6.19)$$

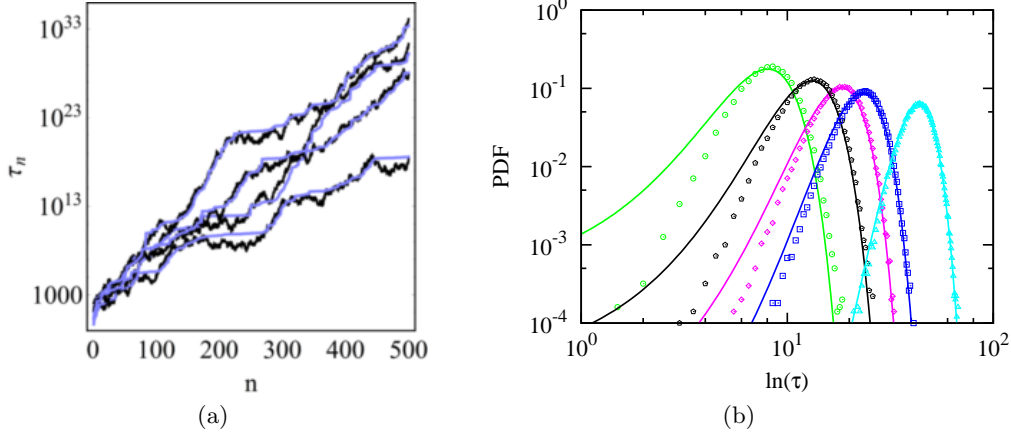


FIGURE 9. (a) Comparison of direct computation (black) and analytic approximation (6.17) (blue) for operational time τ_n with pore number n over four different realizations of the CTRW model. (b) Comparison of the PDF of $\ln \tau$ based upon the analytic approximation (6.19) (solid lines), the PDF of $\ln \tau$ from the CTRW model for (circles) $n = 20$, (pentagons) $n = 40$, (diamonds) $n = 60$, (squares) $n = 80$, (triangles) $n = 160$.

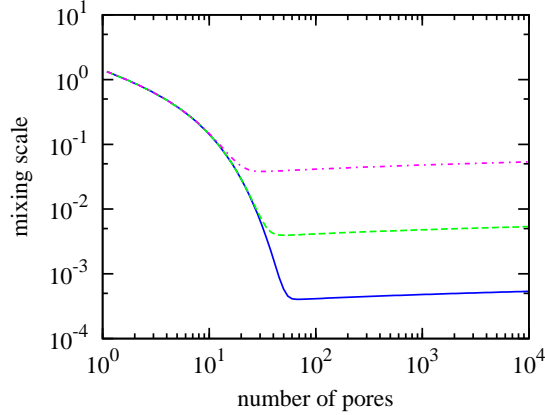


FIGURE 10. Evolution of the average mixing scale (7.3) normalized by σ_0 as a number of pores along the mean flow direction for (dash-dotted) $Pe = 10^4$, (dashed) $Pe = 10^6$ and (solid) $Pe = 10^8$.

with the mean and variance

$$\mu_{\ln \tau}(n) = \langle \ln(t_n) \rangle + n\Lambda_\infty - \ln(n\Lambda_\infty), \quad \sigma_{\ln \tau}^2(n) = 2n\sigma^2. \quad (6.20)$$

Figure 9(b) compares the PDF of ξ_n obtained from evaluating $\tau(t_n)$ according to (6.9) with $\rho(t_n)$ given by the CTRW (5.1) to the approximation (6.19) (with (6.20)), the accuracy of which increases with n due to the central limit theorem.

7. Chaotic Mixing in 3D Random Porous Media

The approximation (6.19) for τ_n provides an accurate solution to the two-step CTRW (5.1), which along with the distribution (4.22) for ρ_n fully quantifies evolution of the concentration distribution, mixing and dilution in the 3D open porous network. In the following we apply this solution to determine evolution of the mixing scale, concentration

PDF, maximum concentration, scalar variance and the onset of coalescence in the 3D random porous network.

7.1. Mixing Scale and Onset of Coalescence

The mixing scale ϵ_m characterizes the distribution of lamellae widths at position $z_n = n$ as

$$\epsilon_m(n) = \frac{\int_{-\infty}^{\infty} d\eta |\eta| c(\eta, t_n)}{\int_{-\infty}^{\infty} d\eta c(\eta, t_n)} = \sigma_0 \frac{\sqrt{2(1 + \tau_n/Pe)}}{\pi \rho_n}, \quad (7.1)$$

the average of which is well approximated by substitution of the approximation (6.17) for τ_n as

$$\langle \epsilon_m(n) \rangle \approx \sigma_0 \left\langle \sqrt{\frac{2(\langle t_n \rangle + Pe \rho_n^{-2})}{\pi n Pe \Lambda_\infty}} \right\rangle, \quad (7.2)$$

Note that whilst $\langle t_n \rangle$ is strictly infinite, the above average is dominated by the bulk of $p_n(t)$, which, as outlined in Appendix A can be well approximated by the Moyal distribution. Thus the average $\langle t_n \rangle$ is understood to be the average of the equivalent Moyal distribution given by (A 14). In order to perform the average over ρ_n , we use a saddle point approximation which yields

$$\langle \epsilon_m(n) \rangle \approx \sigma_0 \sqrt{\frac{2 \ln n}{\pi Pe \Lambda_\infty}} \sqrt{1 + \frac{\ln 2 + \gamma + b}{a \ln n} + \frac{1 - \gamma}{\ln n} + \frac{Pe \exp(-\Lambda_\infty n)}{n \ln n}}. \quad (7.3)$$

This is a remarkable result because although fluid stretching due to pore-scale chaos grows fluid elements exponentially with longitudinal pore number n , the mixing scale does not converge to a constant Batchelor scale with increasing n , but rather increases asymptotically as

$$\langle \epsilon_m(n) \rangle \sim \sigma_0 \sqrt{\frac{2 \ln n}{\pi Pe \Lambda_\infty}}. \quad (7.4)$$

This can be traced back to the broad distribution of arrival times between the couplets arising from the no-slip condition, which renders a distribution of stretching rates of variable strength. Note also, that the characteristic waiting time between stretching events increases with increasing number of couplets, and thus, the stretching rate decreases. This is a characteristic of the Pareto transit time distribution. Figure 10 illustrates the evolution of the average mixing scale given by (7.3) for different Peclet numbers. It assumes a minimum value at a characteristic pore number $n_c \approx \ln Pe / \Lambda_\infty$, at which point diffusive expansion and compression equilibrate.

Whilst the 1D lamellar ADE (6.7) is only valid as long as lamellae are non-interacting, methods are available (Duplat & Villiermaux 2008; Villiermaux 2012; Le Borgne *et al.* 2013) to predict evolution of the scalar concentration field in the presence of coalescence. Whilst such prediction is beyond the scope of this paper, it is important to determine the onset of coalescence and hence the envelope of validity of the model. The onset of coalescence occurs when the mixing scale $\langle \epsilon_m(n) \rangle$ exceeds the average spacing $\epsilon(n) = \pi R^2 / l(n)$ between lamellae of length $l(n) = l_0 \exp(\lambda_\infty n)$ with an initial length l_0 in pores of average radius R . From (7.4), the lamellae are non-interacting up to pore number

$$n + \frac{1}{2\lambda_\infty} \ln \ln n \leq \frac{1}{\lambda_\infty} \ln \left(\frac{\pi R^2}{l_0 \sigma_0} \sqrt{\frac{\pi Pe \Lambda_\infty}{2}} \right), \quad (7.5)$$

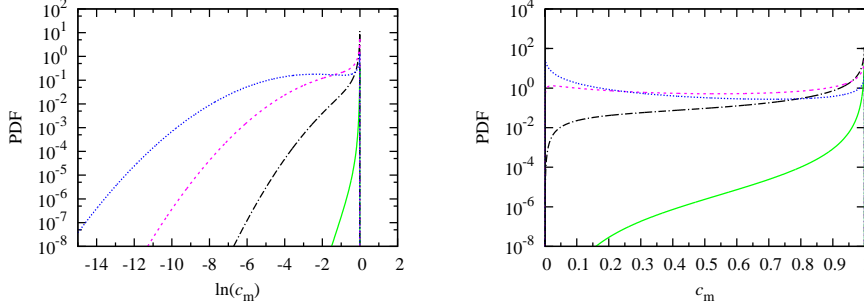


FIGURE 11. PDF (7.9) of (left panel) $\ln c_m$ and (right panel) c_m at downstream positions of (solid) $n = 20$, (dash-dotted) $n = 40$, (long dashed) $n = 60$ and (short dashed) $n = 80$ for $Pe = 10^8$.

where the linear contribution on the LHS of (7.5) is due to exponential stretching of the lamellae, and the weaker nonlinear term is due to evolution of the mixing scale $\langle \epsilon_m(n) \rangle$.

7.2. PDF of Maximum Concentration

The dimensionless maximum concentration $c_m(t)$ as a function of pore number n , $c_m(n) = c_m(t_n)$ is given by (6.14) as

$$c_m(n) = \frac{1}{\sqrt{1 + \tau_n/Pe}}. \quad (7.6)$$

In order to develop an analytic expression for the PDF of $c_m(n) = c_m(t_n)$, we express (7.6) as a function of $\xi_n = \ln(\tau_n)$, which is distributed according to (6.19) as

$$\xi_n = \ln(Pe [c_m(n)^{-2} - 1]), \quad (7.7)$$

hence the PDF $p_m(c_m, n)$ of $c_m(n)$ is then

$$p_m(c_m, n) = \frac{2}{c_m(1 - c_m^2)} p_{\ln \tau} [\ln(Pe [c_m^{-2} - 1])], \quad (7.8)$$

and the PDF of $\zeta_n = \ln[c_m(n)]$ is given by

$$p_{\ln c_m}(\zeta, n) = \frac{2}{1 - \exp(2\zeta)} p_{\ln \tau} [\ln(Pe [\exp(-2\zeta) - 1])]. \quad (7.9)$$

Notice that for $|\zeta| \gg 1$ the PDF of ζ is well approximated by a Gaussian distribution, as per Figure 11 which shows the PDF of $\ln c_m$ for $Pe = 10^8$ at longitudinal distances of $n = 20, 40, 60$ and 80 pores. For small $n \leq 40$, the PDF is sharply peaked about the initial concentration of $c_m = 1$, but for $n > 40$ a peak starts forming away from $c_m = 1$ and the bulk of the probability weight moves away from this initial concentration. This behaviour is reflected by evolution of the mixing scale with n (illustrated in Figure 10), which assumes its minimum at $n_c \approx \ln Pe / \Lambda_\infty$, which for the $Pe = 10^8$ chosen here is $n_c \approx 40$. Thus, once the mixing scale assumes its minimum value, dilution increases markedly due to increased diffusive mass transfer.

The average maximum concentration $\langle c_m(n) \rangle$ shown in Figure 12 evolves in a similar manner; for $n < n_c$ the average maximum concentration $\langle c_m(n) \rangle$ is essentially equal to the initial concentration of 1. For $n \gg n_c$, it decays exponentially rapidly according to

$$\langle c_m(n) \rangle \approx \exp \left[\frac{\sigma_{\ln \tau}^2(n)}{8} - \frac{\mu_{\ln \tau}(n) - \ln Pe}{2} \right], \quad (7.10)$$

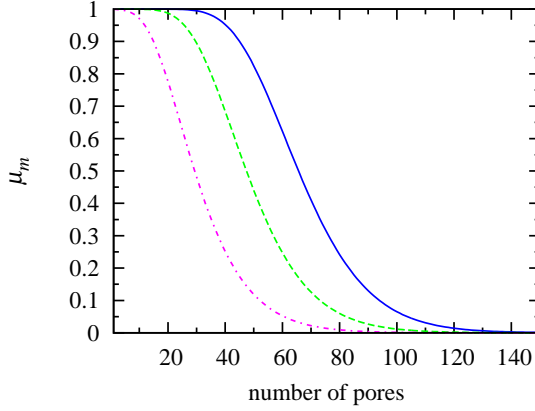


FIGURE 12. Evolution of the average maximum concentration as a number of pores along the mean flow direction for (dash-dotted) $Pe = 10^4$, (dashed) $Pe = 10^6$ and (solid) $Pe = 10^8$.

where $\mu_{\ln \tau}$ and $\sigma_{\ln \tau}^2$ are given by (6.20). Hence exponential fluid stretching due to chaotic advection in 3D porous media generates exponential dilution.

Conversely, fluid deformation in 2D porous media is limited to algebraic stretching as a consequence of the Poincaré-Bendixson theorem. In such media Le Borgne *et al.* (2015) and Dentz *et al.* (2015) find explicitly

$$\mu_{\ln \rho, 2D}(n) = \alpha \ln(n+1) + \sigma_{\ln \rho, 2D}^2(n), \quad \sigma_{\ln \rho, 2D}^2(n) = \beta \ln(n+1), \quad (7.11)$$

where both $\alpha, \beta \in [1/2, 2]$. The mean and variance of the Gaussian $\ln \tau_n$ PDF (6.19) for 2D porous media are then

$$\mu_{\ln \tau, 2D}(n) = \langle \ln(t_n) \rangle + 2\mu_{\ln \rho, 2D}(n) - \ln[2\mu_{\ln \rho, 2D}(n)], \quad \sigma_{\ln \tau, 2D}^2(n) = 4\sigma_{\ln \rho, 2D}^2(n), \quad (7.12)$$

and from (7.10), we obtain the asymptotic algebraic decay of average maximum concentration as $\langle c_{m, 2D}(n) \rangle \propto n^{-\alpha-1/2+\frac{\beta}{2}}$. Hence there exists a qualitative difference in fluid mixing between 2D and 3D porous media: in 2D media fluid stretching is constrained to be algebraic, leading to algebraic dilution, whereas exponential stretching is inherent to 3D porous media, yielding dilution which scales exponentially with longitudinal distance.

7.3. PDF of Concentration

We derive the concentration PDF, mean and variance within the plume as a function of the longitudinal pore number n . As such, this PDF is defined with respect to a support volume that is a subset of the fluid domain which excludes negligible concentrations beyond a minimum cutoff value ϵ . To determine this concentration PDF, we note that the concentration PDF across a single lamella for a given maximum concentration c_m is obtained from (6.11) through spatial mapping as

$$p(c|c_m) = \frac{1}{2c\sqrt{\ln(c_m/\epsilon)\ln(c_m/c)}}, \quad (7.13)$$

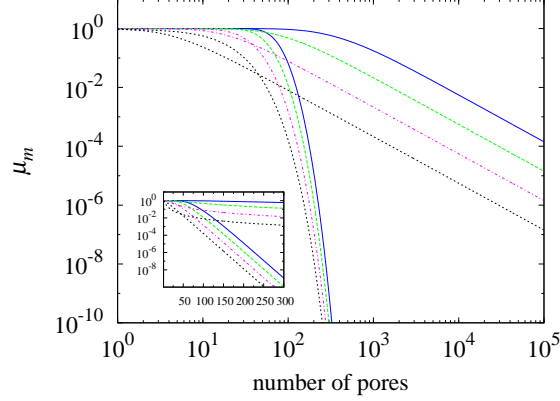


FIGURE 13. Evolution of the average maximum concentration as a function of the number of pores along the mean flow direction for (short-dotted) $Pe = 10^2$ (dash-dotted) $Pe = 10^4$, (long-dashed) $Pe = 10^6$ and (solid) $Pe = 10^8$. The thin lines indicate the 3D pore mixing model, the thick lines, the 2D pore mixing model (7.11)–(7.12) with $\alpha = 1$ and $\beta = 1/5$. The inset illustrates the same plot in a semi-logarithmic scale.

where the concentration range under consideration is $[\epsilon, c_m]$ with ϵ a minimum concentration. The global concentration PDF is then

$$p(c, n) = \int_c^\infty dc_m p(c|c_m) p_m(c_m, n), \quad (7.14)$$

which, using (7.9) and (7.13), may be expressed in terms of the PDF (6.19) of $\ln \tau$ as

$$p(c, n) = \int_{\ln c}^\infty dz \frac{1}{1 - \exp(2z)} \frac{p_{\ln \tau}[\ln(Pe[\exp(2z) - 1]), n]}{c\sqrt{(z - \ln \epsilon)(z - \ln c)}}, \quad (7.15)$$

which may be simplified via a saddle point approximation for $\ln c < \mu_c = \ln \langle c_m \rangle$ to

$$p(c, n) \approx \frac{1}{2c\sqrt{(\mu_c - \ln \epsilon)(\mu_c - \ln c)}}. \quad (7.16)$$

Figure 14 shows the PDFs of $\ln c$ and c from (7.16) for $Pe = 10^8$ as a function of longitudinal pore number n for $n = 20, 40, 60$ and 80 pores. The concentration PDF follows the same trend as that for maximum concentrations in that the PDFs for $n = 20$ and 40 are almost indistinguishable due to limited dilution for $n \leq n_c$ (where $n_c \approx 40$ for $Pe = 10^8$), whereas for significant dilution arises for $n > n_c$ after the mixing scale reaches its minimum.

7.4. Concentration Mean and Variance

The concentration PDF determined in the previous section is obtained by sampling the concentration values $c(x, y, n)$ in space over the concentration support A_c which is defined as $\{\mathbf{x} | c(x, y, n) > \epsilon\}$ where ϵ is the minimum concentration threshold and A_c is a subset of the pore cross-sectional area A . Thus, the concentration PDF may be written as

$$p(c, n) = \frac{1}{A_c(n)} \int_{A_c(n)} d^2 \mathbf{x} \delta[c - c(x, y, n)], \quad (7.17)$$

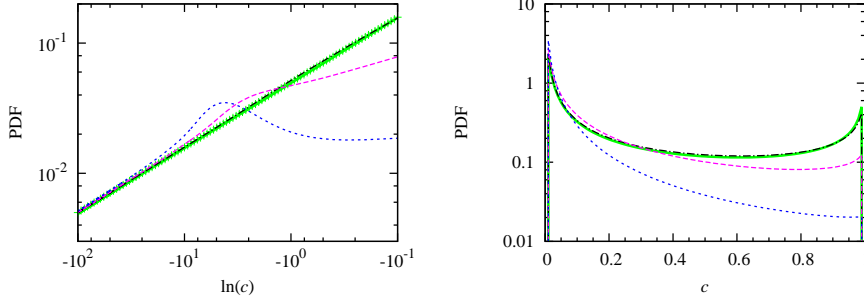


FIGURE 14. PDF of (left panel) $\ln c$ and (right panel) c at downstream positions of (solid) $n = 20$, (dash-dotted) $n = 40$, (long dashed) $n = 60$ and (short dashed) $n = 80$ pores for $Pe = 10^8$.

and the areal concentration support $A_c(n)$ is given by

$$A_c(n) = \int d^2\mathbf{x} H[c(x, y, n) - \epsilon]. \quad (7.18)$$

Whilst the concentration support $A_c(n)$ quantifies mixing within the plume, for some applications it is useful to quantify mixing and dilution over the entire fluid cross-sectional area as support so to quantify global dispersion throughout the pore-space. The decay of such fluid-support spatial variance describes mixing and dilution of the concentration field toward a homogeneous state across the entire pore volume. Conversely, the concentration support measure describes dilution within an evolving plume which deliberately avoids reference to the fluid bulk, hence avoiding the singularity at $c = 0$ in the concentration PDF. We denote the k -th moment of the spatial concentration PDF under the concentration and fluid supports respectively as

$$\langle c(n)^k \rangle \equiv \frac{1}{A_c} \int_{A_c} d\mathbf{x} c(x, y, n)^k, \quad (7.19)$$

$$\overline{c(n)^k} \equiv \frac{1}{A} \int_A d\mathbf{x} c(x, y, n)^k \approx \frac{1}{A} \int_{A_c} d\mathbf{x} c(x, y, n)^k, \quad (7.20)$$

and so these moments are related as $A \overline{c(n)^k} \approx A_c \langle c(n)^k \rangle$ for $\epsilon \ll c_m$. To derive the concentration mean and variance throughout the pore network under both of these measures, we consider the evolution of a single lamella which originates at the injection plane ($z = n = 0$) as a strip of length l_0 with transverse concentration distribution $c(\eta, 0)$ given by (6.8). We pose the spatial distribution of the concentration field after n pores in terms of the material coordinates (η, ζ) , where ζ is the Lagrangian material coordinate along the 1D lamella backbone (shown in Figure 8(b)), the domain of which $\zeta \in [0, l_0]$ references the injected lamella at $z = n = 0$.

Note that the lamella segments distributed throughout a given pore (at fixed z) comprise of contributions from different lamellae injected at $z = n = 0$. Whilst the material coordinate ζ refers to an individual lamella sheet, in the present context we interpret ζ to denote the material coordinate along all of the lamella segments in a given pore, the union of which also span $\zeta \in [0, l_0]$ due to homogeneity of the injection protocol. Whilst this simplification does not extend to inhomogeneous injection protocols such as a point or line source, the homogeneous injection results may readily be generalised to inhomogeneous protocols as per §7.5.

At pore number n the advection time t_n , deformation ρ and operational time τ all

vary with the material coordinate ζ along the lamella, and so we may parameterise these quantities in terms of ζ . Hence the 2D spatial Gaussian concentration distribution (6.7) over the entire lamella may be expressed in material coordinates (η, ζ) as

$$c(\eta, \zeta) = \frac{c_0}{\sqrt{2\pi\sigma_\eta^2(\zeta)}} \exp\left[-\frac{\eta^2\rho(\zeta)^2}{2\sigma_\eta^2(\zeta)}\right], \quad (7.21)$$

where the concentration variance $\sigma_\eta^2(\zeta) = \sigma_0^2 + 2D_m\tau(\zeta)$. The concentration support $A_c(n)$ is quantified by the area of the concentration field for which $c(\eta, \zeta, n) \geq \epsilon$, which corresponds to the cutoff length $\eta_\epsilon(\zeta)$ from the lamellar backbone $\eta = 0$ as

$$\eta_\epsilon(\zeta) \equiv \frac{\sigma_\eta(\zeta)}{\rho(\zeta)} \sqrt{2 \ln \left[\frac{c_m(\zeta, n)}{\epsilon} \right]}, \quad (7.22)$$

and so the concentration mean $\overline{c(n)}$ under the fluid support for $\epsilon \ll c_m(\zeta, n)$ is then

$$\overline{c(n)} \approx \frac{1}{A} \int_0^{l_0} d\zeta \rho(\zeta) \int_{-\eta_\epsilon(\zeta)}^{\eta_\epsilon(\zeta)} d\eta c(\eta, \zeta) = \frac{c_0 l_0}{A} \left\langle \operatorname{erf} \left[\sqrt{\ln \frac{c_m(\zeta, n)}{\epsilon}} \right] \right\rangle \approx \frac{c_0 l_0}{A}. \quad (7.23)$$

Note that the integration over ζ weighted by l_0 is equivalent to performing the average over the ensemble of the elementary lamellae due to the ergodicity of the system as discussed above. As a consequence of (7.23) and (7.19), the concentration support area $A_c(n)$ evolves as

$$A_c(n) \approx \frac{c_0 l_0}{\langle c(n) \rangle}, \quad (7.24)$$

where $A_c(n)$ increases and $\langle c(n) \rangle$ decreases with n as per the concentration support PDF (7.15). The concentration support $A_c(n)$ can be determined by integration along all the lamella segments as

$$A_c(n) = \int_0^{l_0} d\zeta \rho(\zeta) \int_{-\eta_\epsilon(\zeta)}^{\eta_\epsilon(\zeta)} d\eta = \sqrt{\frac{\pi}{2}} \left\langle \frac{c_0 l_0}{c_m(\zeta, n)} \sqrt{2 \ln \left[\frac{c_m(\zeta, n)}{\epsilon} \right]} \right\rangle. \quad (7.25)$$

Thus, it increases approximately as $\langle c_m(n)^{-1} \rangle$.

The difference between the fluid- and concentration-support measures is clearly reflected by the behaviour of the means under these respective measures; under the fluid-support the mean concentration is constant due to conservation, whereas under the concentration support the mean concentration within the plume is decreasing due to plume spreading and dilution. Whilst the result (7.23) holds for all n due to conservation of mass, the derivation above, (7.24) and the PDF (7.15) is only valid in the pre-coalescence regime where A_c does not overlap. To calculate the fluid and concentration support concentration variances

$$\sigma_{\overline{c}}^2(n) \equiv \overline{c(n)^2} - \overline{c(n)}^2, \quad (7.26)$$

$$\sigma_{\langle c \rangle}^2(n) \equiv \langle c(n)^2 \rangle - \langle c(n) \rangle^2, \quad (7.27)$$

under $\epsilon \ll c_m(\zeta)$ we find

$$\int_{-\eta_\epsilon(\zeta)}^{\eta_\epsilon(\zeta)} d\eta c(\eta, \zeta)^2 = \frac{c_0^2}{2\sqrt{\pi}\rho(\zeta)\sigma_\eta(\zeta)} \operatorname{erf} \left[\sqrt{\ln \frac{c_m(\zeta, n)}{\epsilon}} \right] \approx \frac{c_0^2}{2\sqrt{\pi}\rho(\zeta)\sigma_\eta(\zeta)}, \quad (7.28)$$

and so the second concentration moment $\overline{c(n)^2}$ is then

$$\overline{c(n)^2} \approx \frac{\overline{c(n)}}{\sqrt{2}} \frac{1}{l_0} \int_0^{l_0} \frac{c_0}{\sqrt{2\pi\sigma_\eta(\zeta)^2}} d\zeta = \frac{\overline{c(n)}\langle c_m(n) \rangle}{\sqrt{2}} \quad (7.29)$$

where, due to stationarity between pores at fixed n , the average of $1/\sigma_\eta(\zeta)$ along the material coordinate ζ is equivalent to the ensemble average $\langle 1/\sigma_\eta \rangle$. As the maximum concentration $c_m = c_0/\sqrt{2\pi\sigma_\eta^2}$, then the concentration variances may be expressed directly in terms of the average maximum concentration $\langle c_m \rangle$ as

$$\sigma_c^2(n) = \overline{c(n)^2} \left(\frac{\langle c_m(n) \rangle}{\overline{c(n)}\sqrt{2}} - 1 \right), \quad (7.30)$$

$$\sigma_{\langle c \rangle}^2(n) = \langle c(n) \rangle^2 \left(\frac{\langle c_m(n) \rangle}{\langle c(n) \rangle\sqrt{2}} - 1 \right). \quad (7.31)$$

Note that the mean maximum concentration $\langle c_m \rangle$ is neither a fluid- or concentration-support measure but rather is averaged with respect to the 1D manifold comprised of the lamellar segments in the pore cross-section. Whilst (7.30), (7.31) yield negative concentration variances in the homogenization limit of large n (as $\langle c_m(n) \rangle \rightarrow \langle c(n) \rangle \rightarrow \overline{c(n)}$), the derived model is valid in the pre-coalescence regime, and so is not expected to capture the late time dissipation dynamics. Conversely, at earlier times when $\langle c_m(n) \rangle \gg \overline{c(n)}$, $\langle c_m(n) \rangle \gg \langle c(n) \rangle$, both measures of scalar variance evolve in direct proportion to the maximum concentration $c_m(n)$ (7.7), yielding exponential scalar dissipation with pore number n for 3D porous media and algebraic dissipation in 2D media.

7.5. Chaotic Mixing within a Point Injection Plume

Whilst the results above pertain to mixing of a concentration field which is heterogeneous at the pore-scale injected across all pores transverse to the mean flow direction, it is also instructive to consider how these results apply to dilution within a steady solvent plume arising from a continuously injected point source in the 3D random porous network, as illustrated in Figure 4. For a steady plume in homogeneous porous media, the mean macroscopic concentration can be assumed to follow a Gaussian distribution in the direction transverse to the mean flow. Hence, the average lamellar length l_p per pore varies with transverse radial distance r and longitudinal distance $z_n = \ell n$ from the injection source point can be approximated by the 2D Gaussian distribution

$$l_p(n, r) = \frac{l(n)}{2\pi n^2 \sigma_{tr}^2} \exp\left(-\frac{(\varphi r)^2}{2n^2 \sigma_{tr}^2}\right), \quad (7.32)$$

where the total lamellar length is $l(n) = l_0 \exp(\lambda_\infty n)$, φ is the transverse areal porosity, and $\sigma_{tr}^2 = d^2/2$ is the standard deviation associated with a pore branch or merger with centre-to-centre distance d . Such lateral spreading of the plume under continuous point-wise injection significantly retards the onset of coalescence, such that the condition (7.5) is now

$$n + \frac{1}{2\lambda_\infty} \ln \ln n - \frac{(\varphi r)^2}{2\lambda_\infty \sigma_{tr}^2} - \frac{2}{\lambda_\infty} \ln(n\sigma_{tr}^2) \leq \frac{1}{\lambda_\infty} \ln\left(\frac{R^2}{l_0\sigma_0} \sqrt{2\pi Pe\Lambda_\infty}\right). \quad (7.33)$$

Whilst measures with respect to the concentration support A_c such as the mean mixing scale $\langle \epsilon_m(n) \rangle$, maximum concentration $\langle c_m(n) \rangle$, concentration PDF $p(c|n)$, concentration mean $\langle c(n) \rangle$ and variance $\sigma_{\langle c \rangle}^2(n)$ under the concentration support are the same as for point-wise or uniform injection, the concentration mean $\overline{c(n)}$ and variance $\sigma_c^2(n)$ under

the fluid support are markedly different. Following (7.23) and (7.30), these quantities within the plume vary with pore number n and radial distance r as

$$\overline{c_p(n, r)} = \overline{c(n)} \frac{l_p(n, r)}{l(n)}, \quad (7.34)$$

$$\sigma_{c,p}^2(n, r) = \overline{c_p(n, r)}^2 \left(\frac{\langle c_m(n) \rangle}{\overline{c_p(n, r)} \sqrt{2}} - 1 \right). \quad (7.35)$$

Hence the concentration distribution within the plume follows the 2D Gaussian lamellar distribution (7.32), and the rate of scalar dissipation is given by dilution of the maximum concentration $\langle c_m(n) \rangle$ which decays exponentially with pore number n in 3D random media. Note that as $\overline{c_p(n, r)} \ll \langle c \rangle$, the region of validity of (7.35) is significantly larger for the plume injection case. In general (7.34), (7.35) hold for any macroscopic concentration $l_p(x, y, n)/l(n)$ arising from any injection protocol at $n = 0$ in both heterogeneous or homogeneous media.

8. Discussion

The topological complexity inherent to three-dimensional porous media (Vogel 2002) imparts chaotic advection and exponential fluid stretching under steady flow conditions (Lester *et al.* 2013). Such complexity generates a large number density of saddle points in the skin friction field, rendering the associated stable and unstable manifolds which project into the fluid bulk two-dimensional. These 2D surfaces of minimal transverse flux (MacKay 2001, 2008) control transport and mixing, where transverse intersection generates chaotic advection dynamics and persistent exponential fluid stretching as fluid elements are advected through the pore-space. In combination with molecular diffusion, such chaotic advection significantly augments pore-scale mixing and dispersion but has received limited attention.

All porous media (both 2D and 3D, heterogenous and homogeneous) admit no-slip boundaries which impart highly heterogeneous velocity distributions. These distributions determine the frequency of stretching events under advective flow, and the no-slip condition imparts arbitrarily long waiting times between stretching events. We show here that these two basic ingredients of pore-scale topological mixing and heterogeneous advective velocity may be integrated successfully in an analytically tractable stochastic theory that represents fluid deformation as a continuous time random walk (CTRW). The kernels of this CTRW model are quantified via pore-scale computations of fluid deformation and transport in an model 3D random open porous network, and this CTRW model is subsequently coupled to a lamellar model of diffusive mixing to provide quantitative predictions of fluid mixing and dispersion. Although algebraic deformations such as fluid shear also impact mixing, these mechanisms are asymptotically dominated by exponential stretching at the pore-scale.

In the 3D porous network model presented here the no-slip boundary condition generates a Pareto transit time distribution $\psi(\Delta t) \sim \Delta t^{-1-\beta}$ between stretching events, with $\beta = 1$ (5.5). The model can be however readily generalized to other distributions, such as measured in fluid flow simulations through porous media reconstructed from micro-tomography imaging (Bijeljic *et al.* 2011). Chaotic advection arising from steady pore-scale advection generates a log-Gaussian distribution of relative fluid elongation ρ (4.22) transverse to the mean flow direction, the mean of which grows exponentially with longitudinal pore number n as the Lyapunov exponent λ_∞ . The interplay of exponential fluid stretching and Pareto-distributed waiting times leads to an average mixing scale

$\langle \epsilon_m(n) \rangle$ (7.4) which does not converge with n to a constant Batchelor scale, but rather reaches a minimum at $n = n_c \approx \ln Pe / \Lambda_\infty$ and scales asymptotically as $\sqrt{\ln n}$. Consequently, the average maximum concentration $\langle c_m(n) \rangle$ (7.10) and concentration PDF (7.16) within lamellae evolve in a similar fashion, where dilution is negligible up to $n \leq n_c$, but for $n > n_c$ the lamellae then broaden and significant dilution occurs.

The impact of fluid deformation upon fluid mixing and dilution in 2D and 3D porous media is clearly illustrated in Figure 13 by the different scalings for the average maximum concentration $\langle c_m(n) \rangle$ (7.10). In 2D porous media, algebraic fluid stretching leads to fluid mixing which scales algebraically (7.11) with pore number n , whereas the exponential fluid stretching associated with chaotic mixing in random 3D porous media imparts exponential mixing (7.10). This behaviour is directly reflected by evolution of the spatial concentration variance under both fluid-support $\sigma_e^2(n)$ (7.30) and concentration-support $\sigma_{c(n)}^2$ (7.31) measures. These results directly quantify the impact of chaotic mixing in 3D porous media in terms of the pore-scale stretching and advection dynamics.

Whilst this model is only valid up to the coalescence of lamellae as per (7.5), it may be extended as per Duplat & Villermaux (2008); Villermaux (2012); Le Borgne *et al.* (2013) to capture the coalescence regime where mixing is primarily controlled by a diffusive aggregation processes. As mixing dynamics are universally dependent on the rate of fluid deformation, we anticipate that the impact of different fluid stretching dynamics inherent to 2D and 3D random porous media shall persist throughout the coalescence regime.

Application of the CTRW model to a point source solute plume injected shows that chaotic advection again imparts exponential mixing, and the fluid-support concentration variance $\sigma_{c,p}^2(n, r)$ (7.35) is the same as that for the uniform case rescaled by the mean pore concentration $\bar{c}(n, r)$ (7.34). This result is generic to any macroscopic concentration distribution, hence exponentially accelerated mixing persists in both heterogeneous and homogeneous media. Likewise macroscopic longitudinal dispersion is also strongly augmented by chaotic advection (Lester *et al.* 2014). These results have significant implications for the development of macroscopic models of dispersion and dilution which recover the pore-scale mechanisms which arise from chaotic mixing in 3D porous media.

The predictions of concentration PDF and mixing rates from the stretching CTRW model compare very well with fully resolved numerical simulations over a wide range of Peclet numbers for the model 3D open porous network. For extension to real pore-scale architectures, the scalar deformation CTRW framework may be extended to quantify of tensorial fluid deformation via recent developments (Lester *et al.* 2015; Dentz *et al.* 2015) regarding the evolution of the deformation gradient tensor in 3D steady random flows. These developments facilitate statistical characterization of deformation and mixing at the pore-scale and the development of tensorial deformation CTRW models.

9. Conclusions

Three dimensional pore networks are characterized by i) significant topological complexity inherent to all porous media and ii) highly heterogeneous velocity distributions imparted by ubiquitous no-slip conditions at pore walls, further compounded by the distribution of pore sizes. The ubiquity of these mechanisms has significant implications for the prediction and understanding of fluid mixing and macroscopic dispersion in 3D random porous media. The interplay of exponential fluid stretching and broad velocity distributions arising from the no-slip condition generates significantly accelerated mixing via the production of highly striated, lamellar concentration distributions.

We study these mechanisms in a model 3D open porous network which is homogeneous

at the macroscale, and develop a CTRW model for fluid deformation and pore-scale mixing based upon high-resolution CFD simulation of Stokes flow in the network model. Predictions of this model agree very well with direct numerical simulations. Analytic estimates of the mixing dynamics show that mixing and dilution under steady state conditions is controlled by the mean and variance of the fluid stretching rates (quantified respectively by the Lyapunov exponent λ_∞ and the variance σ^2) and the Peclet number Pe , such that the mean concentration decays exponentially with longitudinal advection in 3D random porous media, whereas mean concentration variance decays algebraically in 2D porous media. Whilst highly idealised, these basic mechanisms are universal to 3D porous media and so these results have significant implications for both modelling and understanding mixing in random media.

The developed stretching CTRW model predicts mixing rates for general fluid stretching properties and transit time distributions. Hence, we anticipate that it may be applicable to quantify mixing in a range of porous materials to decipher the role of network topology and structure upon pore scale mixing and thus upon upscaled dilution and mixing-limited reactions. The proposed framework may be extended to transient transport conditions, relevant for instance for pulse tracer injections, through the integration of longitudinal mixing processes.

MD acknowledges the support of the European Research Council (ERC) through the project MHetScale (contract no. 617511), and TLB acknowledges the support of the ERC project ReactiveFronts, and Agence Nationale de la Recherche project Subsurface Mixing and Reaction.

Appendix A. Distribution of Transit Times—The Landau Distribution

The PDF $p_n(t)$ of t_n given in (5.1) can be written in Laplace space as

$$p_n^*(\lambda) = \psi^*(\lambda)^n. \quad (\text{A } 1)$$

The Pareto distribution (5.5) is a Levy-stable distribution, which means in particular that the long time behavior of $p_n(t)$ is the same as the one of (5.5). The Pareto distribution (5.5) reads in dimensionless terms as

$$\psi(\Delta t) = \frac{1}{\Delta t^2}, \quad \Delta t > 1. \quad (\text{A } 2)$$

Its Laplace transform is given by

$$\psi^*(\lambda) = \exp(-\lambda) + \lambda \text{Ei}(-\lambda), \quad (\text{A } 3)$$

where $\text{Ei}(x)$ is the exponential integral (Abramowitz & Stegun 1972). For small $\lambda \ll 1$, this expression can be expanded as

$$\psi^*(\lambda) = 1 - \lambda(1 - \gamma) + \lambda \ln(\lambda) + \dots, \quad (\text{A } 4)$$

where the dots denote subleading contributions of order λ^2 , γ is the Euler constant. Thus, we can write $p_n^*(\lambda)$ for small $\lambda \ll 1$ as

$$p_n^*(\lambda) = \exp[-\lambda n(\ln n + 1 - \gamma) + \lambda n \ln(\lambda n)]. \quad (\text{A } 5)$$

Inverse Laplace transform of this expression, gives for $p_n(t)$ the form

$$p_n(t) = \frac{1}{n} f_1 \left[\frac{t - n(\ln n + 1 - \gamma)}{n} \right], \quad (\text{A } 6)$$

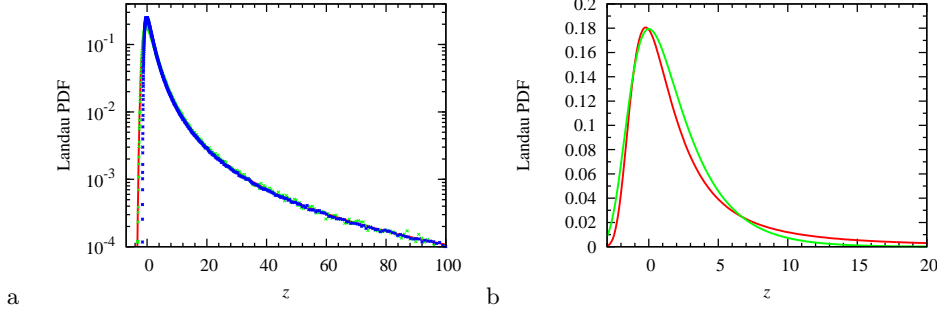


FIGURE 15. Left: Rescaled and shifted PDF $\hat{p}_n(z)$ for (blue) $n = 10$ and (green) $n = 10^3$ obtained from random walk simulations for 10^6 realizations of the stochastic process t_n . The red line indicates the Landau PDF obtained from numerical inverse Laplace transform of (A 7). Right: Comparison of the (red) Landau PDF $f_1(z)$ defined by (A 7) and (green) the approximation (A 10) by the Moyal distribution.

where

$$f_1(t) = \int \frac{d\lambda}{2\pi i} \exp[\lambda \ln(\lambda)] \exp(-\lambda t). \quad (\text{A } 7)$$

denotes the Landau distribution (Uchaikin & Zolotarev 1999). It behaves for $t \gg 1$ as $f_1(t) \approx t^{-2}$. Expression (A 6) describes the density $p_n(t)$ in the limit of large times t or large n . In order to test this approximation, we performed numerical random walk simulations for 10^6 realizations of the random time t_n . The obtained PDF $p_n(t)$ is rescaled as

$$\hat{p}_n(z) = np_n[nz + n(\ln n + 1 - \gamma)], \quad (\text{A } 8)$$

In the limit $n \rightarrow \infty$, we expect $\hat{p}_n(z) \rightarrow f_1(z)$. Figure 15 shows $\hat{p}_n(z)$ for $n = 10$ and 10^3 compared to (A 7), which is obtained by numerical inverse Laplace transform. The maximum of (A 7) is assumed at $t_m = -\frac{1}{2} \ln \frac{\pi}{2}$, as illustrated in Figure 15b.

We consider now the average $\langle \ln t_n \rangle$, which is dominated by the bulk of the Landau distribution $p_n(t)$. To this end, we note that the bulk of the Landau distribution $f_1(t)$ can be approximated by the Moyal distribution

$$f_m(x) = \frac{1}{\sqrt{2\pi}} \exp \left[-\frac{1}{2} (x + e^{-x}) \right] \quad (\text{A } 9)$$

as

$$f_1(t) = af_m[a(t - b)] \quad (\text{A } 10)$$

with $a = 0.7413$ and $b = 0.0064$. Thus, we may approximate $p_n(t)$ in terms of $f_m(x)$ as

$$p_n(t) \approx \frac{a}{n} f_m \left(a \left[\frac{t - n(\ln n + 1 - \gamma)}{n} - b \right] \right) \quad (\text{A } 11)$$

The mean of $\ln t_n$ is then approximated by

$$\langle \ln t_n \rangle \approx \int_{-\infty}^{\infty} dx \ln \left[n(\ln n + 1 - \gamma) + \frac{n}{a} (\langle x_m \rangle + b) + \frac{nx}{a} \right] f_m(\langle x_m \rangle + x), \quad (\text{A } 12)$$

where $\langle x_m \rangle = \ln 2 + \gamma$ is the mean of the Moyal distribution. Thus, we obtain approxi-

mately for $\langle \ln t_n \rangle$

$$\langle \ln t_n \rangle \approx \ln \left[\frac{n}{a} (\ln 2 + \gamma + b) + n (\ln n + 1 - \gamma) \right]. \quad (\text{A } 13)$$

The mean of the $p_n(t)$ as approximated by the Moyal distribution through (A 11) is given by

$$\langle t_n \rangle \approx \frac{n}{a} (\ln 2 + \gamma + b) + n (\ln n + 1 - \gamma). \quad (\text{A } 14)$$

REFERENCES

- ABRAMOWITZ, M & STEGUN, I. A. 1972 *Handbook of Mathematical Functions*. Dover Publications, New York.
- DE ANNA, P., JIMENEZ-MARTINEZ, J., TABUTEAU, H., TURUBAN, R., LE BORGNE, T., DERRIEN, M. & MÉHEUST, Y. 2014 Mixing and reaction kinetics in porous media: An experimental pore scale quantification. *Environ. Sci. Technol.* **48** (508-516).
- DE ANNA, P., LE BORGNE, T., DENTZ, M., TARTAKOVSKY, A. M., BOLSTER, D. & DAVY, P. 2013 Flow intermittency, dispersion, and correlated continuous time random walks in porous media. *Phys. Rev. Lett.* **110**, 184502.
- BAJER, K. 1994 Hamiltonian formulation of the equations of streamlines in three-dimensional steady flows. *Chaos, Solitons and Fractals* **4** (6), 895-911.
- BAJER, K. & MOFFATT, H. K. 1990 On a class of steady confined Stokes flows with chaotic streamlines. *Journal of Fluid Mechanics* **212**, 337-363.
- DE BARROS, F., DENTZ, M., KOCH, J. & NOWAK, W. 2012 Flow topology and scalar mixing in spatially heterogeneous flow fields. *Geophys. Res. Lett.* **39**, L08404.
- BATTIATO, I., TARTAKOVSKY, D. M., TARTAKOVSKY, A. M. & SCHEIBE, T. 2009 On breakdown of macroscopic models of mixing-controlled heterogeneous reactions in porous media. *Adv. Water Resour.* **32**, 1664-1673.
- BERKOWITZ, B., CORTIS, A., DENTZ, M & SCHER, H. 2006 Modeling non-fickian transport in geological formations as a continuous time random walk. *Rev. Geophys.* **44**, RG2003.
- BIJELJIC, BRANKO, MOSTAGHIMI, PEYMAN & BLUNT, MARTIN J. 2011 Signature of non-fickian solute transport in complex heterogeneous porous media. *Phys. Rev. Lett.* **107**, 204502.
- BIJELJIC, B., MUGGERIDGE, A. H. & BLUNT, M. J. 2003 Pore-scale modeling of longitudinal dispersion. *Water Resources Research* **40**, W11501.
- CARRIÈRE, PHILIPPE 2007 On a three-dimensional implementation of the baker's transformation. *Physics of Fluids* **19** (11), 118110.
- CHIOGNA, G., HOCHSTETLER, D.L., BELLIN, A., KITANIDIS, P.K. & ROLLE, M. 2012 Mixing, entropy and reactive solute transport. *geophysical research letters*, 39, doi: 10.1029/2012gl053295. *Geophys. Res. Lett.* **39**.
- CHONG, M. S., MONTY, J. P., CHIN, C. & MARUSIC, I. 2012 The topology of skin friction and surface velocity fields in wall-bounded flows. *Journal of Turbulence* **13** (6), 1-10.
- DENTZ, MARCO, LE BORGNE, TANGUY, LESTER, DANIEL R. & DE BARROS, FELIPE P. J. 2015 Scaling forms of particle densities for Lévy walks and strong anomalous diffusion. *Phys. Rev. E* **92**, 032128.
- DENTZ, M., LE BORGNE, T., ENGLERT, A. & BIJELJIC, B. 2011 Mixing, spreading and reaction in heterogeneous media: A brief review. *J. Cont. Hydrol.* **120-121**, 1-17.
- DUPLAT, J., INNOCENTI, C. & VILLERMAUX, E. 2010 A nonsequential turbulent mixing process. *Phys. Fluids* **22**, 035104.
- DUPLAT, J. & VILLERMAUX, E. 2008 Mixing by random stirring in confined mixtures. *J. Fluid Mech.* **617**, 51-86.
- GRAMLING, C. M., HARVEY, C. F. & MEIGS, L. C. 2002 Reactive transport in porous media: A comparison of model prediction with laboratory visualization. *Environ. Sci. Technol.* **36**, 2508-2514.
- HOLZNER, M., MORALES, V. L., WILLMANN, M. & DENTZ, M. 2015 Intermittent lagrangian velocities and accelerations in three-dimensional porous medium flow. *Phys. Rev. E* **92**, 013015.

- JONES, SCOTT W., THOMAS, ORAN M. & AREF, HASSAN 1989 Chaotic advection by laminar flow in a twisted pipe. *Journal of Fluid Mechanics* **209**, 335–357.
- KANG, P. K., DE ANNA, P., NUNES, J. P., BIJELJIC, B., BLUNT, M. & JUANES, R. 2014 Pore-scale intermittent velocity structure underpinning anomalous transport through 3d porous media. *Geophys. Res. Lett.* **41**, 6184.
- LE BORGNE, T., BOLSTER, D., DENTZ, M., DE ANNA, P. & TARTAKOVSKY, A. 2011 Effective pore-scale dispersion upscaling with a correlated continuous time random walk approach. *Water Resour. Res.* **47**, W12538.
- LE BORGNE, TANGUY, DENTZ, MARCO & CARRERA, JESUS 2008a Lagrangian statistical model for transport in highly heterogeneous velocity fields. *Phys. Rev. Lett.* **101**, 090601.
- LE BORGNE, TANGUY, DENTZ, MARCO & CARRERA, JESUS 2008b Spatial markov processes for modeling lagrangian particle dynamics in heterogeneous porous media. *Phys. Rev. E* **78**, 026308.
- LE BORGNE, T., DENTZ, M. & VILLERMAUX, E. 2013 Stretching, coalescence, and mixing in porous media. *Phys. Rev. Lett.* **110** (20), 204501.
- LE BORGNE, T., DENTZ, M. & VILLERMAUX, E. 2015 The lamellar description of mixing in porous media. *J. Fluid Mech.* **770**, 458–498.
- LESTER, D. R., DENTZ, M., BORGNE, T. LE & BARROS, F. P. J. DE 2015 Protean fluid deformation in three-dimensional steady flow. *Journal of Fluid Mechanics* **in preparation**.
- LESTER, D. R., METCALFE, G. & TREFRY, M. G. 2013 Is chaotic advection inherent to porous media flow? *Phys. Rev. Lett.* **111**, 174101.
- LESTER, D. R., METCALFE, G. & TREFRY, M. G. 2014 Anomalous transport and chaotic advection in homogeneous porous media. *Phys. Rev. E* **90**, 063012.
- MACKEY, R. S. 1994 Transport in 3D volume-preserving flows. *Journal of Nonlinear Science* **4**, 329–354, 10.1007/BF02430637.
- MACKEY, R. S. 2001 Complicated dynamics from simple topological hypotheses. *Philosophical Transactions: Mathematical, Physical and Engineering Sciences* **359** (1784), 1479–1496.
- MACKEY, ROBERT S. 2008 A steady mixing flow with non-slip boundaries. In *Chaos, Complexity and Transport* (ed. C. Chandre, X. Leoncini & G. M. Zaslavsky), pp. 55–68. World Scientific.
- METCALFE, G., SPEETJENS, M.F.M., LESTER, D.R. & CLERCX, H.J.H. 2012 Beyond passive: Chaotic transport in stirred fluids. In *Advances in Applied Mechanics* (ed. Erik van der Giessen & Hassan Aref), *Advances in Applied Mechanics*, vol. 45, pp. 109 – 188. Elsevier.
- MEUNIER, P. & VILLERMAUX, E. 2010 The diffusive strip method for scalar mixing in two dimensions. *J. Fluid Mech.* **662**, 134–172.
- MEZIĆ, I. & WIGGINS, S. 1994 On the integrability and perturbations of three-dimensional fluid flows with symmetry. *Journal of Nonlinear Science* **4**, 157–194.
- MORONI, M. & CUSHMAN, J.H. 2001 Three-dimensional particle tracking velocimetry studies of the transition from pore dispersion to fickian dispersion for homogeneous porous media. *Water Resour. Res.* **37** (4), 873–884.
- OTTINO, J. M. 1989 *The Kinematics of Mixing: Stretching, Chaos, and Transport*. Cambridge, United Kingdom: Cambridge University Press.
- OTTINO, JULIO M. & WIGGINS, STEPHEN 2004 Introduction: mixing in microfluidics. *Philosophical Transactions of the Royal Society of London. Series A:Mathematical, Physical and Engineering Sciences* **362** (1818), 923–935.
- RANZ, W. E. 1979 Application of a stretch model to mixing, diffusion and reaction in laminar and turbulent flows. *AIChE Journal* **25** (1), 41–47.
- SCHOLZ, CHRISTIAN, WIRNER, FRANK, GÖTZ, JAN, RÜDE, ULRICH, SCHRÖDER-TURK, GERD E., MECKE, KLAUS & BECHINGER, CLEMENS 2012 Permeability of porous materials determined from the euler characteristic. *Phys. Rev. Lett.* **109**, 264504.
- SIENA, M., RIVA, M., HYMAN, J.D., WINTER, C.L. & GUADAGNINI, A. 2014 Relationship between pore size and velocity probability distributions in stochastically generated porous media. *Phys. Rev. E* **89** (1), 013018.
- STURMAN, R., MEIER, S. W., OTTINO, J. M. & WIGGINS, S. 2008 Linked twist map formalism in two and three dimensions applied to mixing in tumbled granular flows. *Journal of Fluid Mechanics* **602**, 129–174.

- SURANA, A., GRUNBERG, O. & HALLER, G. 2006 Exact theory of three-dimensional flow separation. part 1. steady separation. *Journal of Fluid Mechanics* **564**.
- TARTAKOVSKY, A. M., REDDEN, G., LICHTNER, P. C., SCHEIBE, T. D. & MEAKIN, P. 2008 Mixing-induced precipitation: Experimental study and multiscale numerical analysis. *Water Resour. Res.* **44**, W06S04.
- UCHAIKIN, V. V. & ZOLOTAREV, M. Z. 1999 *Chance and Stability, Stable Distributions and Their Applications*. Walter de Gruyter.
- VILLERMAUX, E. 2012 Mixing by porous media. *C. R. Mécanique* **340**, 933–943.
- VILLERMAUX, E. & DUPLAT, J. 2003 Mixing as an aggregation process. *Phys. Rev. Lett.* **91**, 18.
- VOGEL, H. J. 2002 Topological characterization of porous media. In *Morphology of Condensed Matter* (ed. Klaus Mecke & Dietrich Stoyan), *Lecture Notes in Physics*, vol. 600, pp. 75–92. Springer Berlin Heidelberg.
- WIGGINS, S. 2010 Coherent structures and chaotic advection in three dimensions. *Journal of Fluid Mechanics* **654**, 1–4.
- DE WINKEL, E.M. & BAKKER, P.G. 1988 *On the Topology of Three-dimensional Viscous Flow Structures Near a Plane Wall: A Classification of Hyperbolic and Non-hyperbolic Singularities on the Wall*. Delft University of Technology, Faculty of Aerospace Engineering.